

MIRACLE II: Unveiling the multi-phase gas interplay in the circumnuclear region of NGC 1365 via multi-cloud modeling

M. Ceci^{1,2}, C. Marconcini^{1,2}, A. Marconi^{1,2}, A. Feltre², I. Lamperti^{1,2}, F. Belfiore², E. Bertola², C. Bracci^{1,2}, S. Carniani³, E. Cataldi^{1,2}, G. Cresci², J. Fritz⁴, M. Ginolfi^{1,2}, E. Hatziminaoglou^{5,6,7}, M. Hirschmann⁸, M. Mingozi⁹, B. Moreschini^{1,2}, F. Mannucci², G. Sabatini², F. Salvestrini^{10,11}, M. Scialpi^{1,2,12}, G. Tozzi¹³, L. Ulivi^{1,2,12}, G. Venturi^{2,3}, A. Vidal-García¹⁴, C. Vignali^{15,16}, and M. V. Zanchettin²

¹ Università di Firenze, Dipartimento di Fisica e Astronomia, via G. Sansone 1, 50019 Sesto F.no, Firenze, Italy
e-mail: matteo.cecini@uni.fi.it

² INAF - Osservatorio Astrofisico di Arcetri, Largo E. Fermi 5, I-50125 Firenze, Italy

³ Scuola Normale Superiore, Piazza dei Cavalieri 7, 56126 Pisa, Italy

⁴ Instituto de Radioastronomía y Astrofísica, Universidad Nacional Autónoma de México, Morelia, Michoacán 58089, Mexico

⁵ ESO, Karl-Schwarzschild-Str. 2, 85748 Garching bei München, Germany

⁶ Instituto de Astrofísica de Canarias, 38205 La Laguna, Tenerife, Spain

⁷ Departamento de Astrofísica, Universidad de La Laguna, 38206 La Laguna, Tenerife, Spain

⁸ Institute of Physics, GALSPEC laboratory, EPFL, Observatory of Saurey, Chemin Pegasi 51, 1290 Versoix, Switzerland

⁹ AURA for ESA, Space Telescope Science Institute, 3700 San Martin Drive, Baltimore, MD 21218, USA

¹⁰ INAF - Osservatorio Astronomico di Trieste, Via Tiepolo 11, I-34131 Trieste, Italy

¹¹ IFPU - Institute for Fundamental Physics of the Universe, via Beirut 2, I-34151 Trieste, Italy

¹² University of Trento, Via Sommarive 14, Trento, I-38123, Italy

¹³ Max-Planck-Institut für Extraterrestrische Physik (MPE), Gießenbachstr. 1, D-85748 Garching, Germany

¹⁴ Observatorio Astronómico Nacional, C/ Alfonso XII 3, 28014 Madrid, Spain

¹⁵ Dipartimento di Fisica e Astronomia, Alma Mater Studiorum, Università degli Studi di Bologna, Via Gobetti 93/2, 40129 Bologna, Italy

¹⁶ INAF-Osservatorio di Astrofisica e Scienza dello Spazio di Bologna, Via Gobetti 93/3, 40129 Bologna, Italy

Received MM dd, year; accepted MM dd, year

ABSTRACT

We present a multi-phase analysis of the gas in the circumnuclear region ($\sim 1.1 \times 1.0 \text{ kpc}^2$) of the nearby barred Seyfert 1.8 galaxy NGC 1365, observed as part of the Mid-IR Activity of Circumnuclear Line Emission (MIRACLE) program. Specifically, we combined spatially resolved spectroscopic data from JWST/MIRI, VLT/MUSE and ALMA to provide a multi-phase characterization of the ionized atomic and the warm and cold molecular gas phases. MIRI data enabled the detection of more than 40 mid-IR emission lines from ionized or warm molecular gas. Moment maps show that both cold and warm molecular gas trace the circumnuclear ring, following the rotation of the stellar disk. The ionized gas exhibits flux distributions and kinematics varying depending on the ionization potential (IP). Low-IP species ($\leq 25 \text{ eV}$) mainly trace the rotating disk, while higher-IP species (up to $\sim 120 \text{ eV}$) trace the outflowing gas. Both $[\text{O III}]\lambda 5007\text{\AA}$ and $[\text{Ne V}]\lambda 14\mu\text{m}$ trace the nuclear outflow cone towards the southeast. In addition, the $[\text{Ne V}]\lambda 14\mu\text{m}$ line traces the counter-cone of the outflow to the northwest, which is obscured in the optical at these circumnuclear scales and thus undetected in $[\text{O III}]\lambda 5007\text{\AA}$. Unlike optical diagnostics, spatially resolved mid-IR diagnostics reveal the key role of the active galactic nuclei (AGN) as the source of gas ionization in the central region. We derive the electron density from the $[\text{Ne V}]\lambda 24\mu\text{m}/[\text{Ne V}]\lambda 14\mu\text{m}$ line ratio, finding a median value of $(750 \pm 440) \text{ cm}^{-3}$, consistent with previous estimates obtained from the optical $[\text{S II}]$ doublet. Lastly, we apply, for the first time, a fully self-consistent combination of state-of-the-art photoionization and kinematic models (HOMERUN+MOKA^{3D}) to estimate the intrinsic physical outflow properties, kinematics, and energetics - overcoming the limitations of classical methods based on oversimplified assumptions. Exploiting the unprecedented synergy between JWST/MIRI and VLT/MUSE, HOMERUN allows us to simultaneously reproduce the fluxes of over 60 emission lines spanning from the optical to the mid-IR. This unique approach enables us to disentangle the physical conditions of AGN- and star formation-dominated components and robustly estimate the mass of the outflowing gas and other physical properties.

Key words. galaxies: Seyfert - galaxies: ISM - galaxies: active - ISM: kinematics and dynamics - ISM: jets and outflows

1. Introduction

Galactic outflows are known to influence the evolution of their host galaxies by removing gas, enriching the circumgalactic medium, and suppressing star formation in the galaxy (Veilleux et al. 2005; Fabian 2012; Cresci & Maiolino 2018; Harrison & Ramos Almeida 2024). While powerful outflows are commonly

observed in luminous active galactic nuclei (AGN) at redshifts $z = 1 - 3$ (e.g., Cano-Díaz et al. 2012; Fiore et al. 2017), similar signatures are also detected in local, less-powerful AGN host galaxies, where high spatial resolution enabled by their vicinity allows for detailed studies of their physical and kinematic properties (Cresci et al. 2015; Venturi et al. 2017, 2018; Cicone et al. 2018; Mingozi et al. 2019; Fluetsch et al. 2019; Lutz et al.

2020). These local outflows span multiple gas phases, from ionized atomic to molecular, and show broad, blue-shifted components in emission and/or absorption lines, consistent with being driven by AGN activity.

Ionized outflows, often traced by strong optical emission lines such as $[\text{O III}]\lambda 5007\text{\AA}$, exhibit velocities ranging from several hundreds to a few thousands km s^{-1} . They are composed of warm gas ($T = 10^4$ K, $n_e = 10^2 - 10^4 \text{cm}^{-3}$) that expands from the nuclear region out to galactic scales, potentially expelling material from their host galaxy (e.g., Harrison et al. 2014, 2016; Woo et al. 2016; Fiore et al. 2017; Venturi et al. 2018; Förster Schreiber et al. 2019; Kakkad et al. 2020; Venturi et al. 2021; Cresci et al. 2023; Speranza et al. 2024; Marconcini et al. 2025b). However, the impact of ionized winds on star formation (SF) remains debated (e.g., Harrison et al. 2016; Harrison & Ramos Almeida 2024), as their coupling efficiency with the ambient interstellar medium (ISM) appears to be low. Indeed, the energy and momentum carried by the ionized gas phase are typically sub-dominant when compared to those of other gas phases (e.g. Zubovas & Bourne 2017; Combes 2017; Fluetsch et al. 2019, 2021; Mulcahey et al. 2022; Belli et al. 2024). In the context of these findings, the ionized gas component may only trace the larger scale, less massive regions of multi-phase outflows, which are dominated in mass by colder molecular or atomic gas on less extended scales (e.g. Ramos Almeida et al. 2022; Audibert et al. 2023; Venturi et al. 2023).

Cold molecular outflows represent a colder phase of gas ($T = 10 - 10^2$ K, $n_e \geq 10^3 \text{cm}^{-3}$), frequently observed via CO emission lines. Compared to the ionized phase, CO-traced outflows are typically slower, with velocities of a few hundred km s^{-1} , but often carry substantial mass, suggesting they may play a crucial role in regulating SF (Feruglio et al. 2010; Fiore et al. 2017; García-Burillo et al. 2019; Lutz et al. 2020; Fluetsch et al. 2019, 2021). In addition to the cold component, warm molecular outflows ($T = 10^2 - 10^3$ K) are typically traced by H_2 roto-vibrational transitions in the near- and mid-infrared (IR). H_2 emission is particularly prominent in shocked regions, making it a sensitive tracer of warm molecular gas entrained in outflows (Hill & Zakamska 2014; Richings & Faucher-Giguère 2018a,b; Riffel et al. 2020; Wright et al. 2023).

NGC 1365, the subject of this work, is a great laboratory to study in detail multi-phase AGN feedback. This dusty barred spiral galaxy (SB(s)b; de Vaucouleurs et al. 1991) is located in the Fornax cluster (Jones & Jones 1980) at a distance of 19.57 Mpc Anand et al. (2021), corresponding to a redshift of $z = 0.005457$ (Bureau et al. 1996). NGC 1365 is classified as a Seyfert 1.8 galaxy (Véron-Cetty & Véron 2006), with signature of both AGN activity and SF in its central regions.

The AGN-driven ionized outflow in NGC 1365 is observed via extended biconical $[\text{O III}]\lambda 5007\text{\AA}$ emission spanning ~ 2.5 kpc, with line-of-sight velocities up to $\pm 170 \text{km s}^{-1}$ (Venturi et al. 2018). The southeastern (SE) cone, approaching the observer, and the receding northwestern (NW) cone - partially obscured by the galactic disk - are dominated by AGN ionization as traced by diagnostic diagrams (Baldwin et al. 1981; Veilleux & Osterbrock 1987; Kewley et al. 2006). High-resolution X-ray observations revealed a fast, highly ionized blue-shifted nuclear (spatially unresolved) wind in absorption with velocities of $\sim 3000 \text{km s}^{-1}$, further supporting the scenario of an AGN-driven wind (Risaliti et al. 2005; Braito et al. 2014).

NGC 1365 has a SF rate of $16.9 M_{\odot} \text{yr}^{-1}$ (Lee et al. 2022), mainly within a ~ 2 kpc radius circumnuclear ring identified across optical, radio, and IR wavelengths (Kristen et al. 1997; Forbes & Norris 1998; Alonso-Herrero et al. 2012). The ring

is associated with the inner Lindblad resonance (Lindblad et al. 1996) and shows non-circular bar-driven gas motions (Teuben et al. 1986; Sanchez 2009), associated with SF-driven ionization (Sharp & Bland-Hawthorn 2010; Venturi et al. 2018) and large reservoirs of molecular gas ($\sim 10^9 M_{\odot}$; Sakamoto et al. 2007; Gao et al. 2021). Observational campaigns from the PHANGS survey (“Physics at High Angular resolution in Nearby Galaxies”, Lee et al. 2023) conducted with the *James Webb* Space Telescope (JWST) and complemented by the Atacama Large Millimeter/submillimeter Array (ALMA; Wootten & Thompson 2009) have revealed that young clusters embedded in the ring drive both ionization of the surrounding medium and localized modifications to the molecular gas phase, where feedback-driven heating and dissociation decrease CO excitation and increase $[\text{C I}]/\text{CO}$ abundance ratios in their immediate vicinity (Liu et al. 2023; Schinnerer et al. 2023).

Despite hints for the presence of a nuclear radio jet in NGC 1365 (Sandqvist et al. 1995), later studies by Stevens et al. (1999) found no conclusive evidence for its presence. Instead, radio emission is primarily attributed to the elongated star-forming ring rather than a jet.

JWST is transforming our understanding of the outflow properties in the local Universe by providing an unprecedented view of the nuclear dusty regions of AGN (e.g. Hermosa Muñoz et al. 2024a; Perna et al. 2024; Zhang et al. 2024; García-Bernete et al. 2024; Davies et al. 2024; Ulivi et al. 2025; Ceci et al. 2025). This revolution is largely driven by the unique capabilities of the JWST Mid-Infrared Instrument (MIRI), including its high spatial resolution across a wide range of wavelengths (from $5 \mu\text{m}$ to $28 \mu\text{m}$), enabling detailed studies of the energetics and kinematics of gas flows in obscured nuclear regions of AGN. The wide IR spectral range of JWST spanning many atomic and molecular gas transitions, combined with its spatial and spectral resolution, provides essential insights into the multi-phase circumnuclear medium. These unprecedented capabilities enable multi-phase, co-spatial analyses when combined with complementary data from ground-based facilities, such as the Multi Unit Spectroscopic Explorer (MUSE) at the ESO Very Large Telescope (VLT; Bacon et al. 2010) and ALMA, transforming our understanding of feedback mechanisms in local AGN.

For NGC 1365, we combine data from the Medium-Resolution Spectrometer (MRS; Rieke et al. 2015; Labiano et al. 2021) of MIRI with integral-field optical spectroscopy from VLT/MUSE and millimeter observations from ALMA. This multi-wavelength approach enables us to trace the multi-phase gas across a wide range of ionization states and densities. In particular, it allows for a detailed characterization of the kinematics, morphology, and energetics of the circumnuclear environment in NGC 1365, ultimately contributing to a deeper understanding of AGN feedback and its impact on galaxy evolution.

This paper is organized as follows. In Section 2, we introduce the observations and the spectroscopic analysis of the MIRI data. In Section 3, we discuss our results through the characterization of the ISM properties and the spatially resolved kinematics of the ionized and molecular gas in the central region of NGC 1365. Finally, in Section 4, we summarize our results. For all the maps shown in this work, north is up and east is to the left.

2. Overview of observations and data analysis

NGC 1365 was observed on 8th December 2024 as part of the “Mid-IR Activity of Circumnuclear Line Emission” (MIRACLE; JWST GO program 6138; Co-PIs: C. Marconcini and A. Feltre), aimed at tracing the mid-IR emission by exploiting

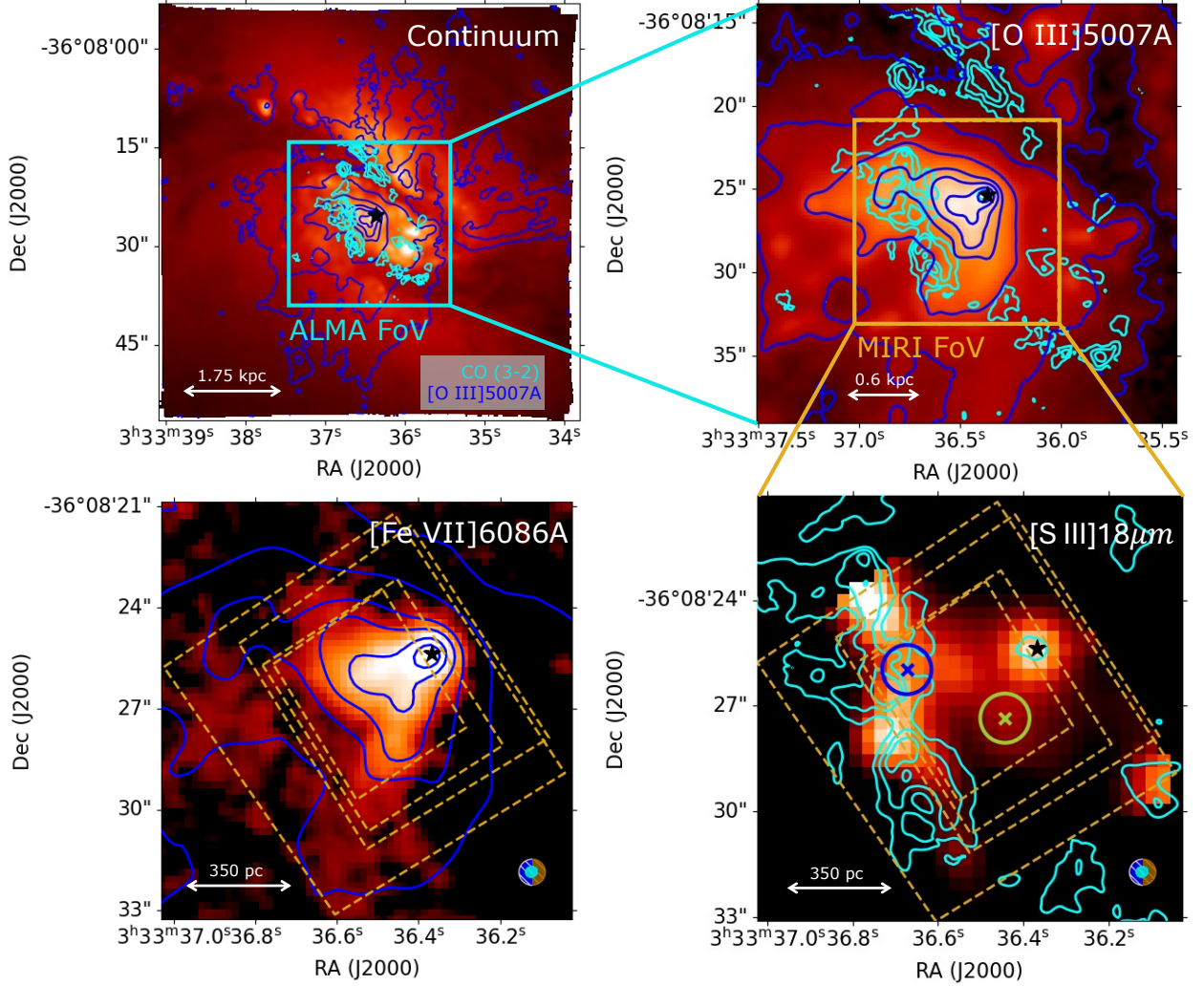


Fig. 1. MIRI, MUSE, and ALMA observations of NGC 1365. *Upper left:* continuum map from MUSE data obtained collapsing the data in the wavelength range 5200–5800 Å. *Upper right:* [O III] λ 5007 Å flux map from MUSE data in the ALMA FoV. *Lower left:* [Fe VII] λ 6087 Å flux map from MUSE data in the MIRI Ch4 FoV. *Lower right:* [S III] $18.51\mu\text{m}$ flux map from MIRI data. Dashed orange rectangles represent the MIRI MRS channels FoV. Blue and green circles of radius of $0.7''$ represent the regions from where we extracted the spectra shown in Fig. 2. Cyan and blue contours represent arbitrary levels of CO(3-2) flux from ALMA and [O III] λ 5007 Å from MUSE, respectively. The star marks the position of the nucleus based on the ALMA data (see Section A.3). In the lower panels, the blue and orange circles represent the MUSE and MIRI PSF, respectively. The ALMA beam is shown as a cyan oval.

MIRI/MRS data of the circumnuclear region of local AGN in the 5–28 μm wavelength range. The MRS mode of MIRI covers a total wavelength range of 4.9–27.9 μm , divided into four integral field units (IFUs), also referred to as channels (Ch1, Ch2, Ch3, and Ch4, hereafter), each further subdivided into three bands (SHORT, MEDIUM, and LONG). These channels cover slightly different fields of view (FoVs), from $3.2'' \times 3.7''$ in Ch1 to $6.6'' \times 7.7''$ in Ch4, at varying pixel size (from $0.13''$ in Ch1 to $0.35''$ in Ch4) and resolving powers (from ~ 3700 to ~ 1500 ; see e.g. Labiano et al. 2021; Argyriou et al. 2023). As shown in Law et al. (2023), the average FWHM of the MIRI/MRS PSF ranges from $\sim 0.4''$ in Ch1 to $\sim 0.9''$ in Ch4. We summarize the data reduction in Appendix A.1, referring to Marconcini et al. (2025a) for a detailed description. As a result of this process, the pipeline produced 12 datacubes, one for each sub-band.

The science observations targeted the nuclear region of NGC 1365 but were deliberately offset to include the inner part of the SE approaching outflow. As shown in the lower panels of Fig. 1, the different MIRI FoVs of each channel are not ex-

actly centered on the nucleus, but shifted toward the SE to better capture the outflow region. This choice was motivated by the primary goal of our MIRACLE project of characterizing multi-phase gas outflows and nuclear properties. In the lower right panel of Fig. 1, we show the nuclear region of NGC 1365 in the MIRI FoV. We extracted integrated spectra from the $0.7''$ radius circular apertures, and we present them in Fig. 2. The green (blue) spectrum is extracted from the circular region shown in Fig. 1 where the outflow (stellar disk) emission is dominant, as shown by the flux maps in Fig. 3. We detected more than 40 emission lines, with a signal-to-noise ratio (SNR) ≥ 5 , in the spectral range covered by MIRI, mostly tracing ionized gas, with an ionization potential IP - defined as the energy required to create the relevant species - ranging from a few eV to more than 100 eV (see Table C.1). Additionally, we also detected two hydrogen recombination lines, namely Pf α and Hu α (i.e. H I (6-5) at 7.46 μm and H I (7-6) at 12.37 μm , respectively) and seven H₂ pure-rotational transitions, from 0-0 S(7) to 0-0 S(1).

As shown in Fig. 2, the MIRI spectra also exhibit at least 15 bright PAH features in the wavelength range between 5 - 18 μm , which we will investigate in a dedicated forthcoming paper. To obtain these spectra, for the first time we combined the emission from all 12 MIRI datacubes, taking into account the different pixel sizes and ensuring a proper flux conservation among different bands by applying a scaling factor to align the flux levels between adjacent bands. A detailed description of this novel procedure is presented in the Appendix B.

In Appendix C.1, we analyzed the MIRI MRS datacubes using a customized python script to enhance the SNR with spatial smoothing, subtract the local continuum around all the brightest emission lines and then fit them spaxel by spaxel. The fitted emission lines are listed in Table C.1.

The MUSE IFU observations of NGC 1365 were obtained on the 12th October 2014, under program 094.B-0321(A) (PI A. Marconi) and are part of the “Measuring AGN Under MUSE” (MAGNUM) survey (Cresci et al. 2015; Venturi et al. 2017, 2018; Mingozi et al. 2019; Marconcini et al. 2023, 2025b). We applied the same data reduction pipeline that has been extensively applied in previous works (e.g. Venturi et al. 2018; Mingozi et al. 2019), and which has been validated and described in detail therein. To trace the cold molecular gas, we used archival ALMA 12-m Band 7 observations (program 2016.1.00296.S, PI F. Combes; Combes et al. 2019) of the CO J=3 \rightarrow 2 transition at 345.796GHz (rest-frame). The observation description, data reduction and emission line fitting procedure of the MUSE and ALMA data can be found in Appendices A.2-C.2 and A.3-C.3, respectively.

3. Results

3.1. Multi-phase gas kinematics

For the kinematic analysis, we focused on emission lines within MIRI Ch3 (0.2"/pixel in a 6.6" \times 7.7" FoV, corresponding to 23 pc/pixel over a 770 \times 900 pc² FoV) because of the good balance between spatial resolution and field coverage. Moreover, the Ch3 emission lines are among the brightest detected in our data, allowing us to present spatially resolved results representative of the ionized and molecular emission, with sufficient SNR across the entire FoV. Although in this analysis we focus on the FoV of Ch3, which also includes a fraction of disk gas illuminated by the AGN and not part of the outflow, it would be more accurate to refer to this region as the ionization cone rather than calling it outflow. However, we will assume in the following that all the gas in the ionization cone is in outflow.

Figure 3 shows the moment maps of [Ne v] λ 14 μm , [Ne II] λ 13 μm , H₂ 0-0 S(1), and CO(3-2), obtained from the emission line fitting routines presented in Appendices C.1 and C.3. The [Ne v] λ 14 μm seems to follow the direction of the ionized outflow, that is, the SE-NW direction (Venturi et al. 2018), as expected from species with high IP (see Table C.1). Its velocity field is also consistent with the [O III] λ 5007Å kinematics, which is blueshifted in the SE and redshifted in the NW. In the SE (NW) cone, we estimate gas projected velocities up to -120 km s⁻¹ (+100 km s⁻¹). The velocity dispersion map of [Ne v] λ 14 μm shows a donut-shaped structure in SE direction of the nucleus (highlighted with contours in Fig. 4), at a projected distance of \sim 2.5" (\sim 300 pc), with a peak of $\sigma \sim$ 170 km s⁻¹.

The lower-IP [Ne II] λ 13 μm emission line has a different morphology with respect to the highly ionized gas traced by the [Ne v] λ 14 μm , suggesting that it traces a different gas component. Indeed, the [Ne II] λ 13 μm morphology resembles the stellar

continuum emission in the circumnuclear ring (whose ALMA contours are highlighted in Fig. 1; see also Liu et al. 2023), as we can see in Fig. 3. Moreover, the moment-0 map reveals bright clumps and lanes in the left part of the FoV that match remarkably well the features visible in H α map of Venturi et al. (2018). This supports the interpretation that the [Ne II] λ 13 μm line predominantly traces the circumnuclear ring. This includes the elongated structure \sim 4" eastward of the nucleus, which is part of the so-called ‘Mid-East’ region - associated with the Southern Arm, a stream of gas flowing in from the southeast along the bar - and is interpreted as material moving downstream within the circumnuclear ring (Liu et al. 2023). The fact that [Ne II] λ 13 μm traces the disk component is also confirmed by the velocity gradient of [Ne II] λ 13 μm , whose direction, along the galaxy disk major axis, and magnitude (\sim 120 km s⁻¹) are consistent with those of the rotating stellar component (and H α) observed on the same scales by Venturi et al. (2018).

The warm molecular gas component, which is traced by the H₂ 0-0 S(1) emission line, shares a similar morphology as that of the [Ne II] λ 13 μm line (Fig. 3). The warm molecular gas flux peaks at larger distances from the nucleus and appears more diffuse, closely resembling the CO(3-2) emission. In contrast, the ionized gas traced by [Ne II] λ 13 μm is concentrated in more compact regions. Since the spatial resolution at the wavelengths of the two lines is comparable, this difference in morphology reflects an intrinsic difference in the extent of the emitting regions. In addition, we observe a concentration of warm molecular gas at the position of the nucleus, which could be explained by the presence of large amounts of dust (as seen in dust continuum from MIRI by Liu et al. 2023) shielding the molecules from the AGN radiation. The kinematics follows the same rotational pattern observed in [Ne II] λ 13 μm , with some deviations from a pure rotating disk. In particular, the NW side of the H₂ velocity map shows lower blueshifted velocities compared to the [Ne II] λ 13 μm velocity. On the opposite side, a deviation from rotation is observed in the redshifted region, which is co-spatial with an enhancement in velocity dispersion. This region, located 2" south of the nucleus, exhibits a peak in dispersion reaching 80 km s⁻¹ and appears as a distinct region.

The CO(3-2) moment maps shown in Fig. 3 are in agreement with the H₂ 0-0 S(1) kinematics, that is tracing the galaxy rotating disk. A similar CO velocity field was reported by Liu et al. (2023). This finding, which is consistent with the lack of any molecular outflow in the circumnuclear region (see also Combes et al. 2019), is in contrast to the CO (1-0) wind reported by Gao et al. (2021). Their outflow interpretation was based on velocity residuals from a rotating disk model on larger spatial scales, which resemble those observed in H α and are more likely due to non-circular inflowing motions along the bar (see their Fig. 6). Notably, the cold gas traced by the CO(3-2) does not show the σ -enhanced region south of the nucleus as the H₂, although both emission lines map the molecular gas. This suggests that the elevated velocity dispersion in H₂ may trace non-circular motions, possibly related to local turbulence or streaming motions induced by the AGN, rather than a genuine outflow. In such an environment, the cold molecular gas traced by CO may not survive due to stronger dissociation or heating, leaving only the warm phase observable in this disturbed region.

The moment maps of the other emission lines listed in Table C.1 are shown in Appendix H, divided into molecular gas, recombination lines, and species with low (< 25 eV), medium (> 25 and < 80 eV), and high (> 80 eV) IP. Grouping such emission lines by IP or gas phase leads to interesting typical patterns. All the H₂ lines share kinematic features similar to those of H₂ 0-

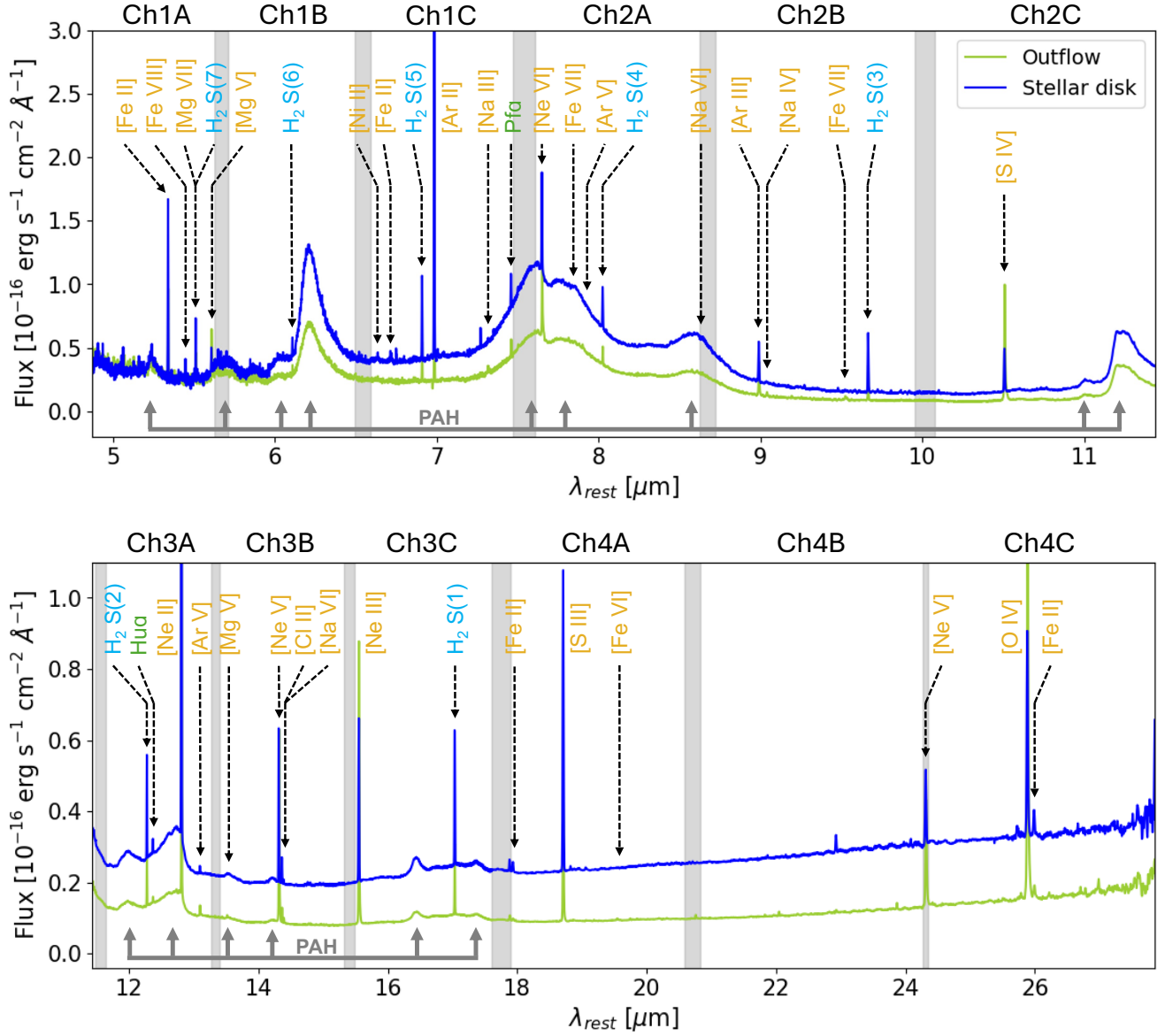


Fig. 2. Integrated spectra of NGC 1365 from MIRI MRS data. The blue and green curves represent the integrated spectra extracted from the $0.7''$ radius apertures marked by the circles in the lower right panel of Fig. 1. These apertures sample regions dominated by the stellar disk and outflow emission, respectively. Detected emission lines are marked with vertical lines: ionized gas emission lines are labeled in yellow, H_2 rotational lines in cyan, and H I recombination lines in green. We annotate the main PAH features with gray arrows. The names of each MIRI MRS sub-channel are indicated, and the gray regions represent the overlapping spectral ranges of two adjacent sub-channels.

0 S(1) in Fig. 3, with a rotational disk kinematics and a high- σ blob to the South of the nucleus. The low IP lines show a velocity gradient consistent with a rotating disk, with an amplitude of $\sim 110 \text{ km s}^{-1}$, like $[\text{Ne II}]\lambda 13\mu\text{m}$. The presence of the high- σ region observed in H_2 is not present in all lines. From the flux maps, we observed that these species are located mainly in the ‘Mid-East’ region (Liu et al. 2023). The moment maps of the high-IP species are similar to those of $[\text{Ne V}]\lambda 14\mu\text{m}$ (see Fig. 3). In particular, the donut-shaped structure is well defined in the velocity dispersion maps, although in the Ch4 the spatial resolution is lower and the shape is not well recognizable. The medium-IP lines have intermediate properties compared to the previous two groups: the velocity gradient is similar to that of the low-IP lines, but the velocity dispersion maps show a high-velocity dispersion region in correspondence of the donut shape.

3.2. Velocity channel maps

Fig. 4 presents the velocity channel maps of the $[\text{O III}]\lambda 5007\text{\AA}$ and $[\text{Ne V}]\lambda 14\mu\text{m}$ emission lines, approximately spanning the velocity range from -500 km s^{-1} to $+550 \text{ km s}^{-1}$ around the same systemic velocity. Both ionic species share the same kinematic structures in each velocity bin, although $[\text{Ne V}]\lambda 14\mu\text{m}$ appears to trace regions closer to the outflow axis, as also found by Mingozzi et al. (2019) for high-ionization gas in MAGNUM galaxies. This is consistent with the fact that both trace the outflow but are associated with different IPs ($\sim 97 \text{ eV}$ and $\sim 35 \text{ eV}$ for $[\text{Ne V}]$ and $[\text{O III}]$, respectively; see Table C.1). Indeed, $[\text{Ne V}]\lambda 14\mu\text{m}$ emission arises from more internal regions of the outflow, where the AGN radiation field is expected to be stronger. Interestingly, Fig. 3 shows that at projected velocities larger than 100 km s^{-1} , the $[\text{Ne V}]\lambda 14\mu\text{m}$ emission resem-

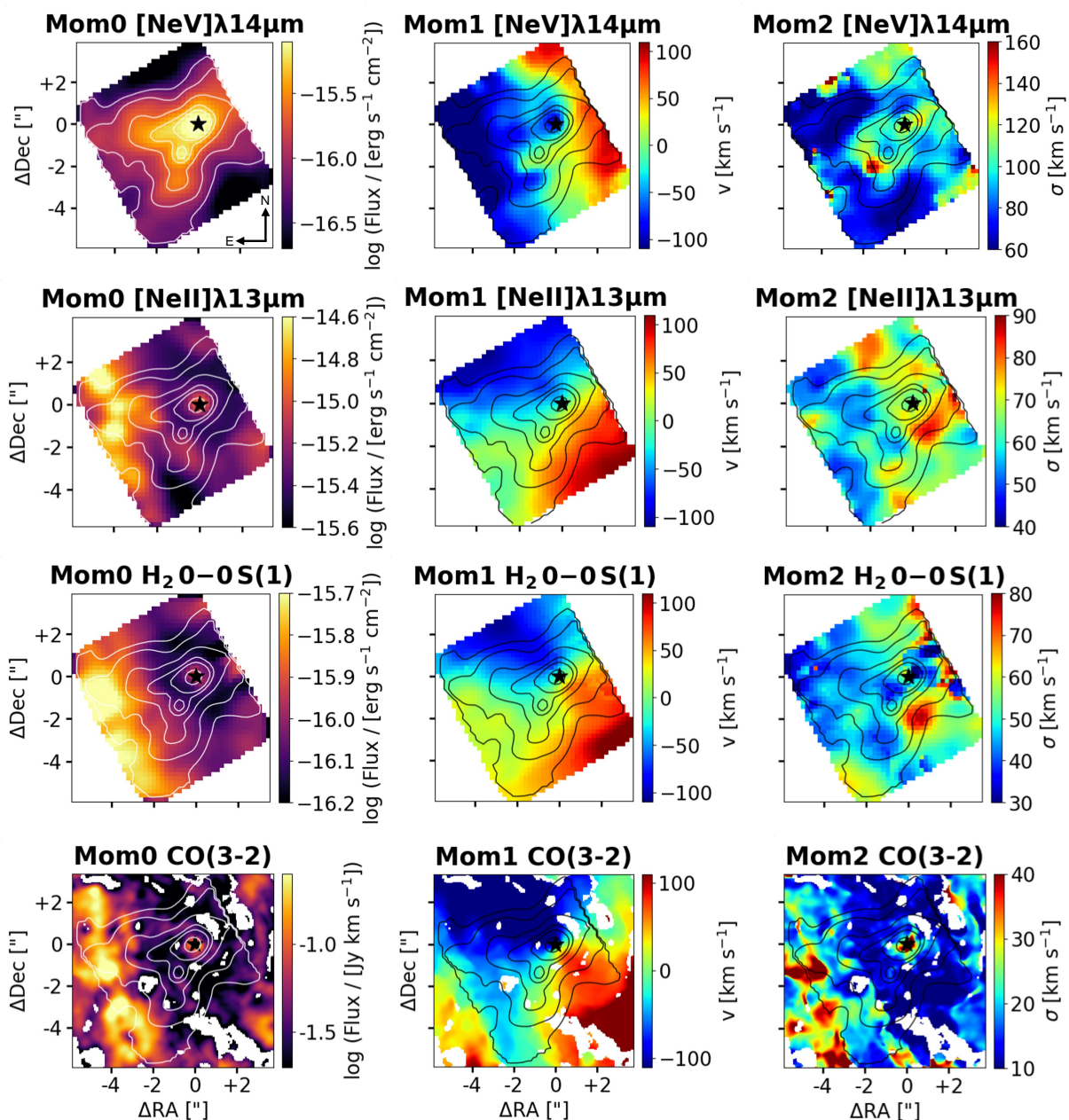


Fig. 3. Moment maps of ionized and molecular gas emission in NGC 1365, tracing both the rotating disk and the outflowing gas components. From top to bottom: $[\text{Ne v}]\lambda 14\mu\text{m}$, $[\text{Ne II}]\lambda 13\mu\text{m}$, $\text{H}_2 0-0 \text{S}(1)$, and $\text{CO}(3-2)$ moment maps. From left to right, we show the flux, the line-of-sight velocity, and the velocity dispersion map. The contours represent arbitrary flux levels of $[\text{Ne v}]\lambda 14\mu\text{m}$ emission. The star marks the nucleus position. The maps size is $1100 \times 1120 \text{ pc}^2$. Spaxels with $\text{SNR} < 5$ are masked.

bles the donut-shaped structure mentioned above. The bulk of the emission progressively shifts away from the nucleus with increasing channel velocity, tracing the lower arm of the donut-shaped structure. Moreover, unlike $[\text{O III}]\lambda 5007\text{\AA}$, the redshifted $[\text{Ne v}]\lambda 14\mu\text{m}$ velocity channels clearly reveal the receding NW ionization cone, which is otherwise highly obscured in the optical due to dust in the galaxy disk. Indeed, as discussed in the following, the NW cone lies behind the disk and suffers stronger extinction than the SE cone (Venturi et al. 2017, 2018; Marconcini et al. 2025b). Thanks to the lower dust attenuation in the mid-IR, the $[\text{Ne v}]\lambda 14\mu\text{m}$ line is an optimal tracer of this obscured outflowing component.

3.3. Resolved diagnostic diagrams for gas excitation

Diagnostic diagrams featuring mid-IR emission line ratios are widely used to investigate the nature of the gas ionizing sources (e.g. Hao et al. 2009; Weaver et al. 2010; Inami et al. 2013; Richardson et al. 2022; Martínez-Paredes et al. 2023; Feltre et al. 2023; Garofali et al. 2024; Mingozzi et al. 2025). In particular, to map the gas excitation within the circumnuclear region of NGC 1365 we exploited the mid-IR line ratios recently explored by Feltre et al. (2023) within local AGN, exploiting Spitzer integrated spectra including NGC 1365. To account for the different FoVs, pixel sizes, and point spread functions (PSFs) of each sub-channel, we corrected each flux map of the mentioned emission lines accordingly before computing the ratios. Specifically, we adopted the smallest FoV ($6.6'' \times 7.7''$, i.e. Ch3), the

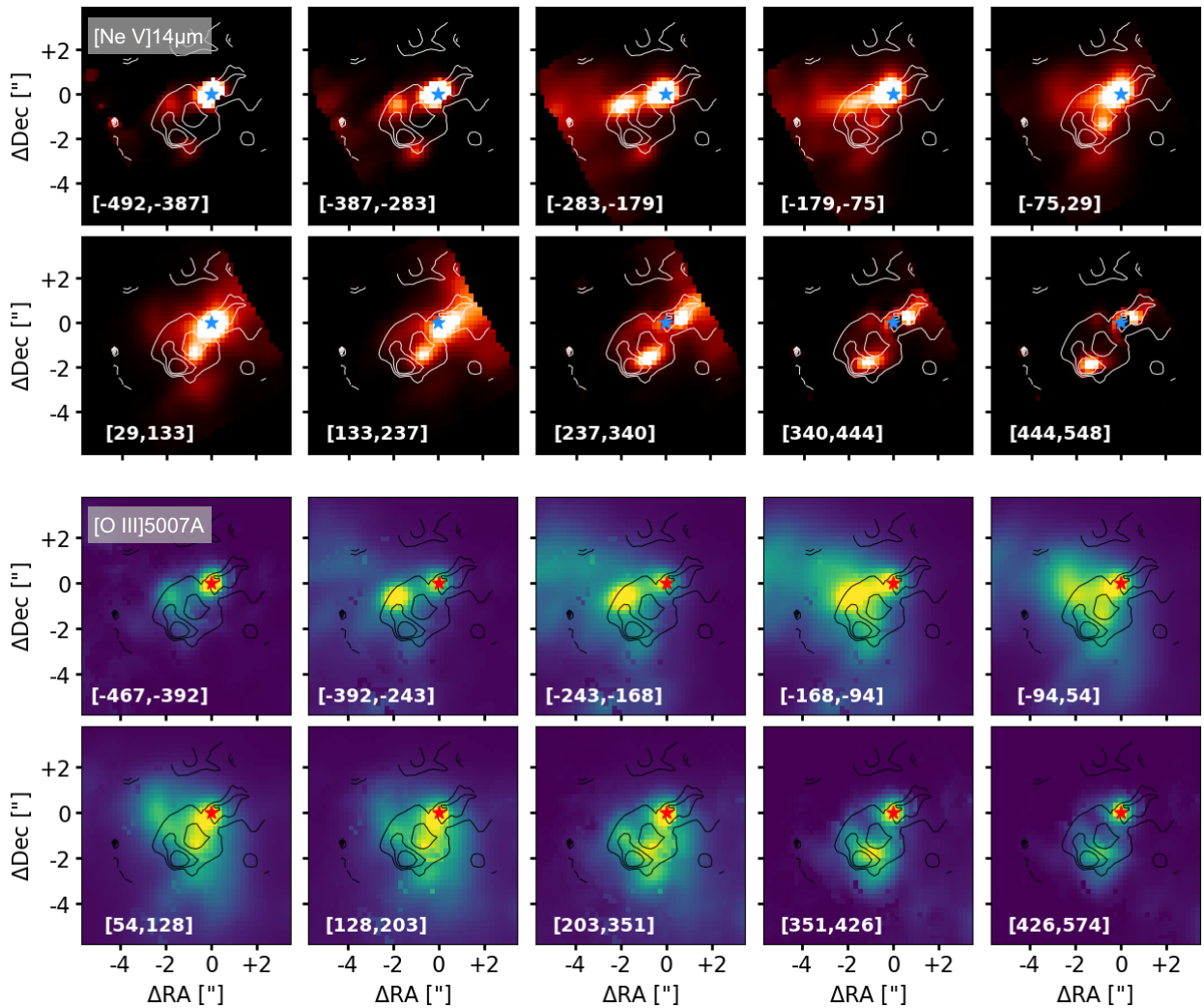


Fig. 4. Channel maps of ionized gas species tracing the outflow kinematics from MIRI and MUSE data. *Upper panel:* channel maps of $[\text{Ne V}]\lambda 14\mu\text{m}$ emission lines from MIRI data. *Lower panel:* channel maps of $[\text{O III}]\lambda 5007\text{\AA}$ emission from WFM MUSE data. Contours indicate velocity dispersion levels of 97, 114, and 130 km s^{-1} in the $[\text{Ne V}]\lambda 14\mu\text{m}$ emission. Velocity bins are indicated at the top of every panel in km s^{-1} and are computed relative to the same systemic velocity. The star marks the position of the nucleus based on the ALMA data (see Section A.3).

largest pixel size ($0.35''$ from Ch4), and convolved all images to the worst PSF (i.e. $\sim 1.0''$, the one at the reddest wavelength of $\sim 26\mu\text{m}$). Additionally, as detailed in Appendix B, we applied multiplicative correction factors to account for flux discontinuities between the datacubes (see Fig. B.2).

In the upper left panel of Fig. 5, we show the contours of line ratio model predictions for AGN (Feltre et al. 2023), SF galaxies (Gutkin et al. 2016), and shocks (Alarie & Morisset 2019) for the $[\text{O IV}]\lambda 26\mu\text{m}/[\text{Ne II}]\lambda 12\mu\text{m}$ and $[\text{Ne III}]\lambda 15\mu\text{m}/[\text{Ne II}]\lambda 12\mu\text{m}$ line ratios. We include all available model grids, applying only a metallicity cut of $Z > 0.006$ (see Feltre et al. 2023 for further details on the models). We overlay our data on model predictions, where each pixel is color-coded based on its position in the corresponding diagnostic diagram. This diagram shows that the main ionization source in the circumnuclear region of NGC 1365 can either be shocks or AGN, while no evidence for SF excitation is detected. According to Fig. 5 of Feltre et al. (2023), adding fractional contributions from SF and shock models to an AGN model will shift the points towards the bottom-left in the diagram. Therefore, we classify as shock- or AGN-excited only those spaxels that fall entirely within a single predicted region. Data points located in overlapping or unclassified regions cannot

be uniquely attributed to a single excitation mechanism. To better visualize the spatial distribution and morphology of these regions, we produce diagnostic maps using the same color-coding of the diagrams, as shown in the lower panels of Fig. 5.

In the central column of Fig. 5, we show the $[\text{Ne III}]\lambda 15\mu\text{m}/[\text{Ne II}]\lambda 12\mu\text{m}$ versus $[\text{Ne V}]\lambda 14\mu\text{m}/[\text{Ne II}]\lambda 12\mu\text{m}$ diagnostic diagram. Similarly to the $[\text{O IV}]$ diagram, the data points are separated into shock- and/or AGN-excited models. The $[\text{O IV}]$ and $[\text{Ne V}]$ excitation maps reveal similar spatial structures: an extended region dominated by AGN and combined shock/AGN excitation, aligned with the disk major axis and delimited on either side by shock-dominated zones. Notably, the eastern shock front coincides with the edge of the circumnuclear ring traced by CO and $\text{H}\alpha$ (see Fig. 3 and Venturi et al. 2018), which may indicate that the outflow, emerging from the disk, shocks the material of the circumnuclear ring along its path. In contrast, the centrally elongated feature may reflect direct AGN ionization within the disk.

Exploiting optical MUSE data, we compare the mid-IR diagnostic diagrams with the optical $[\text{S II}]$ BPT diagram (Kewley et al. 2006, 2013) shown in the right column of Fig. 5. Moreover, we also considered the $[\text{N II}]$ and $[\text{O I}]$ BPT diagrams, finding

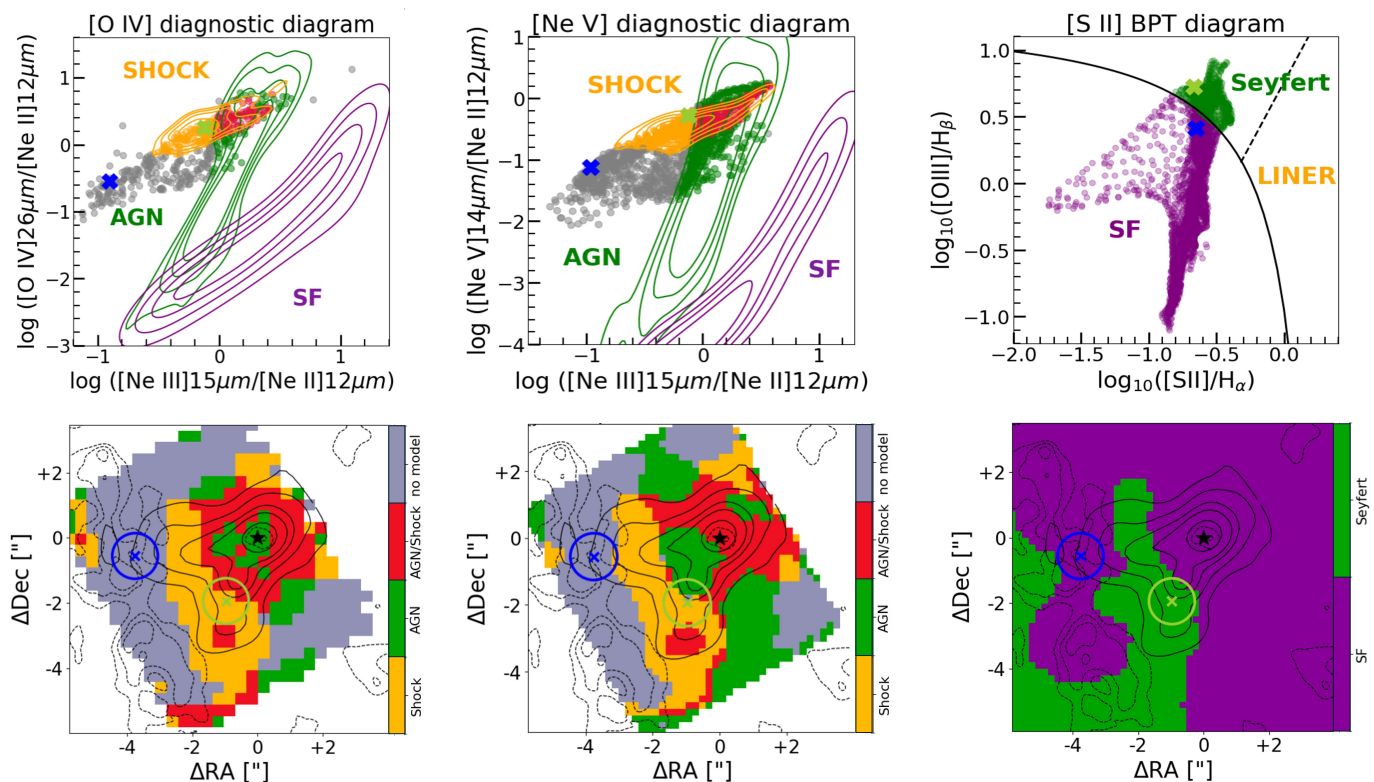


Fig. 5. Comparison between mid-IR and optical diagnostic diagrams. Top panels, from left to right: diagnostic diagram of $[\text{Ne III}]\lambda 15\mu\text{m}/[\text{Ne II}]\lambda 12\mu\text{m}$ vs $[\text{O IV}]\lambda 14\mu\text{m}/[\text{Ne II}]\lambda 12\mu\text{m}$, $[\text{Ne III}]\lambda 15\mu\text{m}/[\text{Ne II}]\lambda 12\mu\text{m}$ vs $[\text{Ne V}]\lambda 14\mu\text{m}/[\text{Ne II}]\lambda 12\mu\text{m}$, and $[\text{S II}]\lambda\lambda 6716, 6731/\text{H}\alpha$ vs $[\text{O III}]\lambda 5007\text{\AA}/\text{H}\beta$. In the mid-IR diagnostic diagrams, data points are color-coded by their proximity to the SF-, AGN-, and shocks-excitation models, based on the predictions by [Feltre et al. \(2023\)](#). In the $[\text{S II}]$ BPT diagram, the solid curve defines the theoretical upper bound for pure SF ([Kewley et al. 2001](#)), while the dashed one separates Seyfert galaxies from LINERs ([Kewley et al. 2006](#)). The lower panels show spatially resolved excitation maps, where each pixel is color-coded based on its position in the corresponding diagnostic diagram. In the mid-IR diagnostic diagrams, shocks-excited spaxels are in orange, AGN-excited spaxels in green, overlapping spaxels are in red, and spaxels not reproducible with any single model are in gray. In the $[\text{S II}]$ BPT diagram, Seyfert-excited spaxels are in green, and SF-excited spaxels are in purple. Solid black contours represent arbitrary $[\text{Ne V}]\lambda 14\mu\text{m}$ flux levels, while dashed black contours represent arbitrary levels of CO(3-2) flux from ALMA data. Circles are the regions where colored crosses in the upper panels and spectra in [Fig. 2](#) are extracted from, integrated with a radius of $0.7''$. The star marks the position of the nucleus based on the ALMA data (see [Section A.3](#)). Spaxels with SNR < 10 are masked.

similar results (see [Fig. 5](#) in [Venturi et al. 2018](#) and [Appendix D3](#) in [Mingozzi et al. 2019](#) for these diagrams at large scale). As found by [Venturi et al. \(2018\)](#), we notice that the circumnuclear SF ring seen in $\text{H}\alpha$ and in CO (see [Fig. 1](#)) is not fully dominated by SF in the BPT diagrams. Instead, as visible from the $[\text{S II}]$ spatial distribution, certain regions in the SE of the nucleus show signatures of AGN excitation. [Venturi et al. \(2018\)](#) conclude that this is likely due to the superposition along the line of sight of the AGN-ionized cone and the SF ring. The main difference between the optical BPT and the mid-IR diagnostic diagrams we presented lies in their ability to trace the true ionization source in dusty environments. In the nuclear region, the optical BPT appears to be dominated by star formation due to strong dust obscuration, as indicated by the Balmer decrement (see [Appendix D](#) and [Fig. D.1](#)). In contrast, mid-IR diagnostics can penetrate the dust screen and clearly reveal AGN ionization at the nucleus. This explains why, in the optical, AGN ionization cones are only visible on larger spatial scales, as previously shown in [Venturi et al. \(2018\)](#) and [Mingozzi et al. \(2019\)](#). Another notable difference is that the region classified as shock-dominated in the mid-IR diagrams appears to be excited by the AGN radiation according to the optical diagnostic diagram. This discrepancy likely reflects the different depths probed by optical and mid-IR emission, with mid-IR lines tracing higher ionization

regions deeper into the disk, where shocks from the interaction between the outflow and the disk are expected to occur.

3.4. Electron density estimation

One of the main advantages of MIRI is the availability of mid-IR density-sensitive line ratios, such as $[\text{Ne V}]\lambda 24\mu\text{m}/[\text{Ne V}]\lambda 14\mu\text{m}$. These ratios are sensitive to a higher density regime with respect to the commonly used optical $[\text{S II}]\lambda 6716/[\text{S II}]\lambda 6731$ ratio, due to the different ionization energies and critical densities of the lines involved. Recent studies used IR tracers to explore the gas density in local Seyfert galaxies and found densities in the range $\log(n_e/\text{cm}^{-3}) = 3-5$ ([Hermosa Muñoz et al. 2024b,a](#); [Zhang et al. 2024](#); [Ceci et al. 2025](#); [Ramos Almeida et al. 2025](#)).

In the top panel of [Fig. 6](#), we show the electron density map derived from the $[\text{Ne V}]\lambda 24\mu\text{m}/[\text{Ne V}]\lambda 14\mu\text{m}$ ratio using PyNeb ([Luridiana et al. 2015](#)), assuming an electron temperature $T_e = 10^4$ K (following typical values adopted for ionized gas in AGN narrow-line regions; [Osterbrock & Ferland 2006](#)). Across the FoV, we estimate a median electron density of $\log(n_e/\text{cm}^{-3}) = (2.7 \pm 0.5)$, with a peak of $\log(n_e/\text{cm}^{-3}) \sim 3.5$ at the nucleus. The density cannot be computed in some spaxels where the $[\text{Ne V}]$ line ratio exceeds the lower density limit (LDL) of ~ 1.2 . In these spaxels, we can assume an upper limit for the density

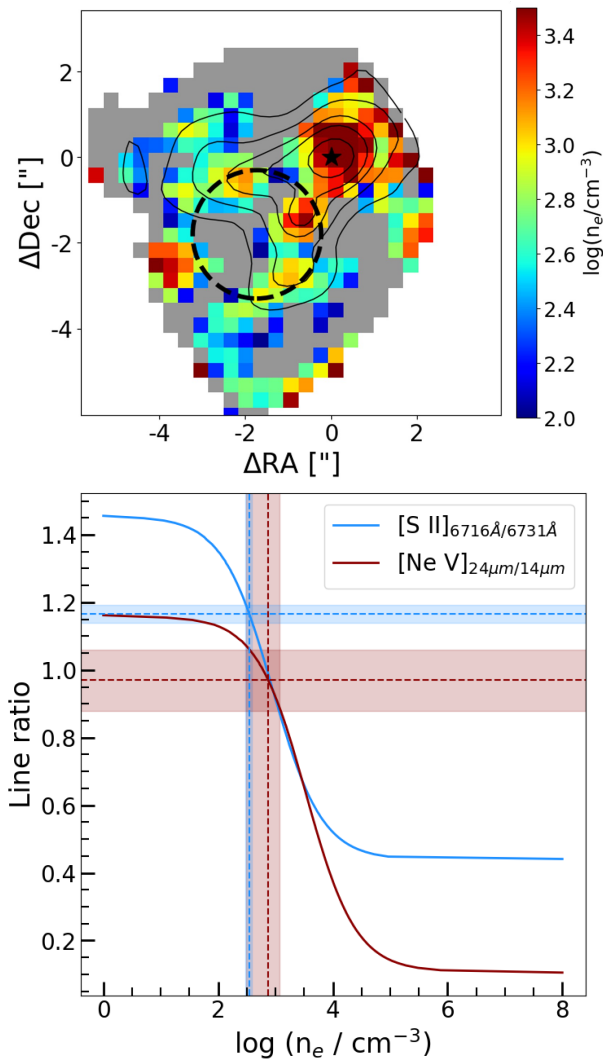


Fig. 6. Density map from [Ne v] and comparison with [S II]-based values. *Top panel:* electron density map derived from the [Ne v] $\lambda 24\mu\text{m}/[\text{Ne v}]\lambda 14\mu\text{m}$ line ratio. Gray pixels indicate regions where the observed ratio exceeds the theoretical low-density limit (LDL) of ~ 1.2 . In these spaxels, we can assume an upper limit for the density of $\log(n_e/\text{cm}^{-3}) \leq 2$. Black contours trace arbitrary flux levels of [Ne v] $\lambda 14\mu\text{m}$ emission. The black circle marks the $1.5''$ radius aperture used to extract integrated densities from [S II] and [Ne v]. Spaxels with SNR < 10 are masked out. *Bottom panel:* theoretical [S II] and [Ne v] line ratios as a function of electron density, computed with PyNeb (Luridiana et al. 2015). Vertical dashed lines indicate the density values in the circular aperture inferred from the observed ratios (shown as horizontal dashed lines) and shaded regions represent the errors.

of $\log(n_e/\text{cm}^{-3}) \leq 2$. In the remaining regions, the morphology of the density map appears to follow the conical structure of the outflow, as traced by the [Ne v] $\lambda 14\mu\text{m}$ emission line (see Fig. 3).

Additionally, as shown in Appendix D, we computed the electron density map from the [S II] $\lambda\lambda 6716, 6731$ doublet observed in the MUSE data (see Venturi et al. 2018 and Mingozi et al. 2019 for the maps in the entire MUSE FoV). Both the circumnuclear ring and the outflow region are characterized by peaks in electron density, with values reaching $\log(n_e/\text{cm}^{-3}) \sim 2.6\text{--}2.8$. This spatial distribution is consistent with the findings of Venturi et al. (2018) and Kakkad et al. (2018), who reported enhanced electron densities in similar structures.

For a quantitative comparison between the optical and mid-IR tracers, we measured the electron density from integrated spectra extracted within a $1.5''$ (~ 126 pc) radius aperture centered on the outflow region (see Fig. 6), using both the mid-IR and optical tracers. From the mid-IR [Ne v] line ratio, we estimate an electron density of $(750 \pm 440) \text{ cm}^{-3}$, while from the [S II] lines we find a consistent value of $(350 \pm 40) \text{ cm}^{-3}$. These values are illustrated in the bottom panel of Fig. 6, where we plot the theoretical [S II] and [Ne v] line ratios as functions of electron density using PyNeb (Luridiana et al. 2015), assuming an electron temperature $T_e = 10^4$ K.

Based on our analysis, the gas density derived from the mid-IR diagnostics is ≈ 0.3 dex higher than the one derived from the optical, although consistent within the error. This difference is in agreement with the findings of Ramos Almeida et al. (2025), who reported similar, or even larger, offsets in a sample of five Type-2 quasars. Following Ramos Almeida et al. (2025), we also attribute this discrepancy to the different physical conditions probed by the two tracers: optical lines such as [S II] $\lambda\lambda 6716, 6731$ are more sensitive to diffuse, lower-density gas, while mid-IR fine-structure lines trace denser and more obscured regions, typically located closer to the AGN and less affected by dust extinction.

Our attempt to compute n_e from the [Ar v] $\lambda 13\mu\text{m}/[\text{Ar v}]\lambda 8\mu\text{m}$ ratio within the $1.5''$ -radius aperture interestingly yielded a ratio of ~ 2.1 , which is above the [Ar v] LDL value of ~ 1.8 (corresponding to an upper limit on $\log(n_e/\text{cm}^{-3})$ density similar to the [Ne v] one, ~ 2). More importantly, even when integrating the [Ne v] flux across the entire MIRI FoV, we do not observe line ratios falling in the low-density limit (LDL), contrary to what was found by Dudik et al. (2007) using Spitzer/IRS data. This further supports the idea that their higher [Ne v] $\lambda 24\mu\text{m}/[\text{Ne v}]\lambda 14\mu\text{m}$ ratios - and apparent detection of LDL conditions - may originate from observational limitations. In particular, the higher sensitivity of JWST/MIRI MRS compared to Spitzer/IRS may have allowed for a more effective detection of low surface brightness emission that could have remained undetected in previous studies. A direct comparison with the Dudik et al. (2007) measurements and observational setup is presented in Appendix E.

3.5. Photoionization modeling with HOMERUN

We model the full set of optical to mid-IR emission using state-of-the-art photoionization models. Specifically, we employed the Highly Optimized Multi-cloud Emission-line Ratios Using photo-ionization (HOMERUN) modeling framework developed by Marconi et al. (2024).

3.5.1. Model grids of AGN and SF

Given the superposition along the line of sight of the AGN-ionized cone and the circumnuclear SF ring, in the HOMERUN fit we combined two suites of models: one reproducing the emission of dust-free gas ionized by the AGN, and another accounting for the SF contribution, modeled as emission from dusty nebulae around H II regions and including both dust depletion and dust physics. Both components were assumed to have the same metallicity; however, while we adopted dust-free models for the AGN component, we included dust in the SF models and corrected gas-phase metallicities using the depletion factors listed in Table 7.8 of Hazy 1 (Cloudy v23.1). This choice was motivated by the optical extinction map (Appendix D), which shows clear

dust structures associated with the SF ring, but not with the outflowing AGN-ionized gas. Furthermore, the AGN-ionized component exhibits iron coronal lines, indicating that at least part of the dust has been destroyed, releasing iron into the gas phase.

Specifically, the shape of the AGN ionizing radiation field is described by a power law with UV slope $\alpha_{UV} = -0.5$, an exponential cutoff $\exp(-h\nu/k T_{\text{Max}})$ and the X-ray component slope of $\alpha_X = -1.0$ linked to the UV through the α_{ox} . We have computed models with following combinations of $\log(T_{\text{Max}}/\text{K}) = 4.0, 4.5, 5.0, 5.5, 6.0, 6.5, 7.0$ and $\alpha_{ox} = -1.2, -1.5, -1.8$.

As described in Marconi et al. (2024), the incident spectra for the SF model grids are stellar population models from BPASS v2.3 (Byrne et al. 2022; Stanway & Eldridge 2018) including binary stellar evolution. These models use a Kroupa (2001) initial mass function and an upper mass cut-off of $300 M_{\odot}$. We select models with solar value for the stellar metallicity $\log(Z_{\text{star}}) = -1.7$ and ages in $\log(\text{age}/\text{Myr})$ of 6.0, 6.4, 6.6, 7.1, 8.8.

The other model parameters are identical for the two suites of models (AGN and SF), namely the ionization parameter U (i.e., the number of ionizing photons compared to that of atoms of neutral hydrogen) ranges from -4.0 to -0.5 in step of 0.5 and the hydrogen density of the gas, $\log(N_{\text{H}} / \text{cm}^{-3})$ from 0 to 7 in steps of 1. For the first iteration HOMERUN spans metallicities $\log(Z/Z_{\odot})$ from -1.0 to 0.4 in steps of 0.2. After this first iteration, HOMERUN performs a final refinement in steps 0.02 on predictions interpolated across the finer grid.

3.5.2. HOMERUN modelling approach

The HOMERUN models the line emission with a weighted combination of multiple CLOUDY single-cloud photoionization models (Ferland et al. 1998), iterating over different gas metallicities and incident radiation fields. The novelty of this method is that the weights assigned to the individual single-cloud models are treated as free parameters during the fitting process.

As explained in detail in Marconi et al. (2024), the fitting process starts by selecting a grid of CLOUDY models, defined by hydrogen density (n_{H}) and ionization parameter (U) for a fixed ionizing spectrum (S_{ν}), gas phase oxygen abundance (A_{O}), and elemental abundance ratios (Z). For each such grid, the code searches for the best-fitting multi-cloud model by combining individual single-cloud templates. This is achieved by solving a Non-Negative Least Squares (NNLS) problem, where the weights of each cloud are constrained to be non-negative. The procedure is conceptually analogous to stellar population fitting methods (e.g., pPXF; Cappellari & Emsellem 2004), where a galaxy spectrum is reproduced as a linear combination of stellar templates with positive weights. No regularization is applied in the minimization, allowing for full flexibility in the weight distribution. The process is repeated across all available grids, spanning different ionizing continua, metallicities, and abundance scalings. The optimal solution is identified as the one minimizing the loss function $L_{\text{min}}(S_{\nu}, A_{\text{O}}, Z)$, which quantifies the deviation between model predictions and observed emission-line fluxes. This loss function is effectively a reduced χ^2 statistic, so values ≤ 1 indicate a statistically good fit.

When exploring different metallicities, elemental abundances were scaled from the solar photospheric values of Asplund et al. (2021), except for carbon and nitrogen, which were rescaled following the prescriptions of Nicholls et al. (2017). During the fit, all elemental abundances except oxygen were allowed to vary from their initial values. Scaling factors were used for the AGN and SF components, which could be different for refractory elements but the same for non-refractory ones.

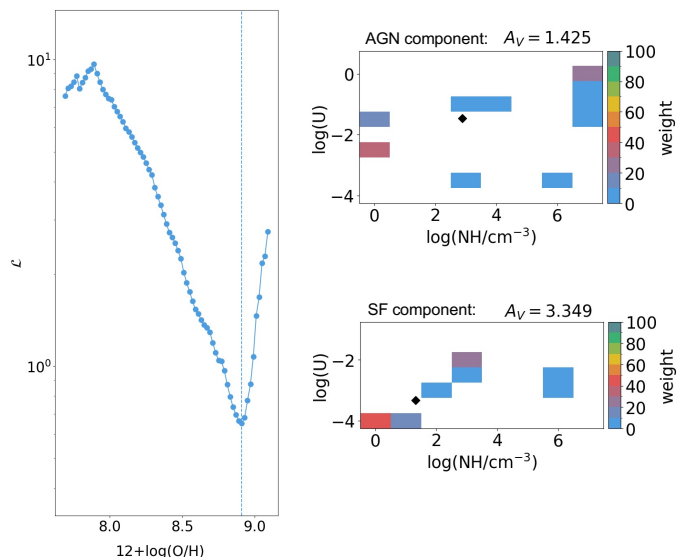


Fig. 7. HOMERUN model results using two component. *Left panel:* variation of the loss function \mathcal{L} as a function of the oxygen abundance, $12+\log(\text{O}/\text{H})$. In this scale, the solar metallicity is 8.69. The blue vertical dashed line represents the metallicity of the model with the minimum value of \mathcal{L} . *Right panels:* grids of single-cloud models in $\log(U)$ and $\log(N_{\text{H}})$ for the two components of the fit. The colors represent the weights of each single-cloud model, as indicated by the color bar, when \mathcal{L} reaches the minimum value. The black diamond represents the weighted density and ionization parameter of the single-cloud models.

3.5.3. HOMERUN fitting results

We fit the fluxes of 60 ionized and neutral atomic emission lines measured from the MIRI and MUSE spectra (32 from MIRI and 28 from MUSE, see Figs. 2 and A.1) extracted within a $1.5''$ radius aperture centered on the outflow region (see Fig. 6). The unique approach of HOMERUN enables us to reproduce at the same time 60 different emission lines in different ionisation stages, with the majority of them reproduced with better than 15% accuracy. The data are best matched by a SF component with mean $A_{\text{V}} = 3.3$, $\log(n_{\text{H}} / \text{cm}^{-3}) = 1.3$, and $\log(U) = -3.3$ and an AGN component with mean $A_{\text{V}} = 1.4$, $\log(n_{\text{H}} / \text{cm}^{-3}) = 2.9$, and $\log(U) = -1.4$ (see Fig. 7). Being results of ionized gas region, in the following we will consider $n_{\text{H}} = n_{\text{e}}$.

We find that the SF component is more dust-attenuated than the outflow, in agreement with the extinction map obtained from the Balmer decrement (see Fig. D.1) where the higher A_{V} values trace the circumnuclear ring and the nucleus. Interestingly, the difference in A_{V} between SF and AGN components is in line with the median values found in MAGNUM galaxies dividing the emission in disk and outflow (Mingozi et al. 2019). In Section 3.4, we computed the electron density from the mid-IR $[\text{Ne v}]$ and the optical $[\text{S II}]$ line doublet ratios within the same $1.5''$ radius aperture. The density derived from $[\text{Ne v}]$, $\log(n_{\text{e}}/\text{cm}^{-3}) \sim 2.87$, is consistent with the average value of the AGN model components, $\log(n_{\text{e}}/\text{cm}^{-3}) = 2.9$. This is expected since HOMERUN attributes the entire emission of $[\text{Ne v}]$ to the AGN (see Table F.2), as stars may not produce hard-enough radiation to account for the emission of this transition. Conversely, the $[\text{S II}]$ lines yield a relatively higher density of $\log(n_{\text{e}}/\text{cm}^{-3}) \sim 2.5$ within the $1.5''$ radius aperture, compared to $\log(n_{\text{e}}/\text{cm}^{-3}) \sim 1.3$ from HOMERUN. This is because the average density of the SF component from HOMERUN is lower than that from the $[\text{S II}]$ doublet and HOMERUN requires a contribu-

tion of more than 70% from the SF component to reproduce the [S II] emission (see Table F.1). This highlights the strength of our decomposition method: while classical [S II] diagnostics measure a global electron density, HOMERUN disentangles the different ionizing sources and shows that the SF component alone has a much lower density. Finally, the derived ionization parameters are $\log(U) = -1.4$ for the AGN component and a lower $\log(U)$ of -3.3 for the SF component, both in line with values found in H II regions (e.g. Kewley et al. 2001; Dopita et al. 2006) and AGN narrow-line regions (e.g. Groves et al. 2004). This supports the effectiveness of our decomposition in isolating distinct ionization regimes.

Figure 7 shows the results of the fit. The left panel shows the behavior of the loss function as a function of oxygen abundance. The minimum of the curve is found for the minimum loss function of $\mathcal{L}_{\min} = 0.6$, corresponding to $12 + \log(O/H) = 8.91$. The left panels represent the weights of the single-cloud models with different U and N_H which were derived for the best fit, for the AGN and SF components in the upper and lower panel, respectively. Using the weights, it is possible to compute the average density and ionization parameter of the clouds, which are identified by the black filled diamond. Only a small number of single-cloud models have non-zero weights, and the AGN and SF components contribute differently across the various lines, depending on the ionization state. In particular, as indicated in Tables F.1 and F.2, high-ionization lines (e.g., Ne V, O III) are predominantly reproduced by the AGN component, while lower-ionization lines (e.g., N II, Cl II, Ar II) are mainly explained by the SF component. Interestingly, the H α luminosity is produced more than 70% by AGN excitation.

3.5.4. Ionized gas mass from HOMERUN

A key outcome of the HOMERUN fitting procedure is the ability to relate the luminosity of an emission line to the mass of the ionized gas associated. Since the fit is based on a physically consistent combination of AGN and SF single-cloud models, it allows us to disentangle the contributions from the different ionizing sources and connect the observed emission to intrinsic gas properties. In this way, under the assumption that the outflowing gas is fully ionized by the AGN, we avoided including the contribution from systemic or SF-related components, ensuring that the derived masses trace the outflowing gas itself. In particular, for each component, HOMERUN provides both the intrinsic (i.e., extinction-corrected) luminosities (see Tables F.1 and F.2) and the corresponding ionized gas mass. From the underlying single-cloud CLOUDY models, one obtains for each model a surface brightness in H β (i.e. $\log L_{H\beta}/\text{area}$) and a gas mass surface density (i.e. $\log M_{\text{ion}}/\text{area}$). These model outputs define a direct proportionality between H β luminosity and ionized gas mass. By rescaling this relation to the total luminosity of a specific emission line (e.g., [Ne V] or [O III]) and taking into account the AGN fraction f_{AGN} as determined from the HOMERUN fit, we derive a general expression:

$$M_{\text{ion}} = C_{\text{line}} \times \frac{L_{\text{line}}}{f_{\text{AGN}}}, \quad (1)$$

where C_{line} is a calibration coefficient derived from the HOMERUN AGN component models. This framework provides a robust and physically grounded method to estimate the mass of ionized outflowing gas from spatially integrated line luminosities.

After applying HOMERUN to NGC 1365 emission line fluxes, we found the following ionized mass:

$$M_{[\text{O III}]} = 0.74 \times 10^5 M_{\odot} \left(\frac{L_{\text{AGN}}([\text{O III}])}{10^{40} \text{ erg s}^{-1}} \right) \quad (2)$$

$$= 3.0 \times 10^5 M_{\odot} \left(\frac{L_{\text{obs}}([\text{O III}])}{10^{40} \text{ erg s}^{-1}} \right), \quad (3)$$

$$M_{[\text{Ne V}]} = 4.4 \times 10^5 M_{\odot} \left(\frac{L_{\text{AGN}}([\text{Ne V}])}{10^{40} \text{ erg s}^{-1}} \right) \quad (4)$$

$$= 3.0 \times 10^5 M_{\odot} \left(\frac{L_{\text{obs}}([\text{O III}])}{10^{40} \text{ erg s}^{-1}} \right), \quad (5)$$

where $L_{\text{AGN}}([\text{O III}])$ and $L_{\text{AGN}}([\text{Ne V}])$ are the intrinsic line luminosities emitted by the AGN component, and $L_{\text{obs}}([\text{O III}])$ and $L_{\text{obs}}([\text{Ne V}])$ are the total observed luminosities (i.e. without the HOMERUN separation between AGN and SF). The scaling factors applied to the observed luminosities account for both the fractional contribution of the AGN component and the effect of reddening. The scaling factors of L_{AGN} in Equations 2 and 4 refer to extinction-corrected luminosities and can be directly compared with the standard conversion factors adopted in analytical calculations of the ionized gas masses (Equations G.5 and G.6, see also the discussion in the next section).

We compute an outflow mass of $M_{[\text{Ne V}]} = (109 \pm 2) \times 10^3 M_{\odot}$ and $M_{[\text{O III}]} = (88 \pm 9) \times 10^3 M_{\odot}$ within the $1.5''$ radius aperture. These differences in mass, obtained with HOMERUN, reflect the discrepancy between the observed and model-predicted line ratios. Indeed, the observed ratio between [O III] $\lambda 5007\text{\AA}$ and [Ne V] $\lambda 14\mu\text{m}$ fluxes is 0.81 times the model ratio (see Appendix F), which matches the ratio between the [O III] $\lambda 5007\text{\AA}$ - and [Ne V] $\lambda 14\mu\text{m}$ -based outflow masses. We emphasize that the scaling relations in Equations 2-5 for the ionized outflow masses are not universally applicable to other AGN. They are derived specifically from the HOMERUN multi-cloud modeling customized for the physical conditions and emission properties of NGC 1365. Therefore, applying these relations to other galaxies requires performing a dedicated HOMERUN fit tailored to the individual characteristics of each galaxy.

3.6. Outflow energetics

We compare the outflow mass obtained with HOMERUN modeling in the previous section with that estimated following a standard and commonly used approach (e.g. Cano-Díaz et al. 2012; Carniani et al. 2015, see Appendix G). This classical method relies on several strong assumptions, such as considering that all the species are in the ionization state responsible for the observed line (e.g. O $^{2+}$ for [O III], Ne $^{4+}$ for [Ne V]), adopting a single average density (from [S II] in the optical and [Ne V] in the mid-IR), and correcting for attenuation using the Balmer decrement.

With HOMERUN we obtain an outflow mass of $M_{[\text{Ne V}]} = (109 \pm 2) \times 10^3 M_{\odot}$ and $M_{[\text{O III}]} = (88 \pm 9) \times 10^3 M_{\odot}$ within a $1.5''$ radius aperture centered on the outflow region (see Fig. 6 and Section 3.5.3). In addition, following Carniani et al. (2015), in Appendix G we present a detailed derivation of the outflow mass of [Ne V] $\lambda 14\mu\text{m}$ and [O III] $\lambda 5007\text{\AA}$. Overall, with the classic method we find in the same spatial region $M_{[\text{Ne V}]} = (2.6 \pm 1.0) \times 10^3 M_{\odot}$ and $M_{[\text{O III}]} = (20 \pm 7) \times 10^4 M_{\odot}$. The large difference between the HOMERUN and classical mass estimates (factors of ~ 40 for [Ne V] and ~ 2 for [O III]) clearly

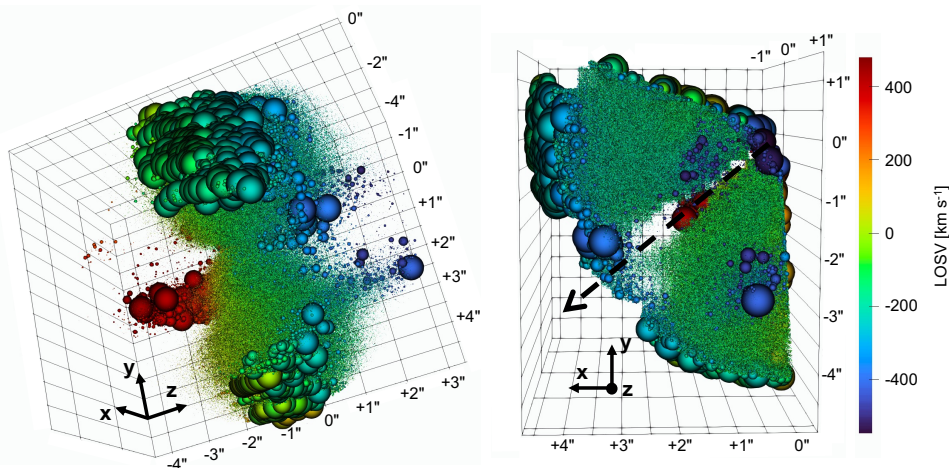


Fig. 8. 3D reconstruction of the MOKA^{3D} best-fit model of the ionized outflow traced by [Ne v] λ 14 μ m. Gas clouds are color-coded by their line-of-sight velocity (LOS_V). The two panels show different viewing angles: the left one provides a view into the inner cone region, while the right one corresponds to the observer’s line of sight. The XY plane represents the plane of the sky, and the Z axis is the line of sight. In the right panel, the dashed arrow indicates the direction of the conical outflow axis. According to the colorbar, blue and red clouds are blue-shifted and red-shifted, respectively. Bubble size scales with the intrinsic flux of each cloud.

highlights the fundamental limitations of the standard approach. The classical method relies on several strong assumptions, such as considering that all the species are in the ionization state responsible for the observed line (e.g. O²⁺ for [O III], Ne⁴⁺ for [Ne v]), adopting a single average density (from [S II] in the optical and [Ne v] in the mid-IR), and correcting for attenuation using the Balmer decrement. In contrast, HOMERUN does not require assumptions about ionization levels, temperature, or metallicity, and accounts for differential reddening between the two components. The reliability of the more complex HOMERUN approach is demonstrated by the fact that classical method mass estimates differ by a factor of ~ 75 between different tracers, highlighting the inherent inconsistencies of the traditional approach. Indeed, for example, the HOMERUN fitting shows that the fraction of neon in the form of Ne⁴⁺ in the best-fit models is only $\sim 10\%$, while for O²⁺ the fraction is significantly higher, around 60% of the total oxygen. This is certainly one of the main factors contributing to the large discrepancy between the two mass estimates.

We assume that the flux density within each spaxel is constant over time and that the outflow subtends a solid angle Ω . Therefore, we compute the mass outflow rate as $\dot{M}_{\text{out}} = M_{\text{out}} v_{\text{out}} / \Delta R$, i.e. the amount of ionized mass crossing a distance ΔR with velocity v_{out} . We also calculate the outflow kinetic energy as $E_{\text{out}} = \frac{1}{2} \dot{M}_{\text{out}} v_{\text{out}}^2$ and the outflow power as $P_{\text{out}} = \frac{1}{2} \dot{M}_{\text{out}} v_{\text{out}}^2$.

We infer the [Ne v] λ 14 μ m and [O III] λ 5007 \AA intrinsic (i.e. de-projected) radial velocities of the outflow (v_{out}) using the 3D multi-cloud MOKA^{3D} kinematic model (Marconcini et al. 2023). This model has demonstrated exceptional power in reproducing outflow features with unprecedented detail, leveraging IFU data from a variety of instruments (Marconcini et al. 2023; Cresci et al. 2023; Perna et al. 2024; Ulivi et al. 2025; Marconcini et al. 2025a,b). To reproduce the outflow features in NGC 1365, we adopted a conical outflow morphology with maximum extension of 5 arcsec (420 pc) and position angle¹ of 235°. The free parameters of the fit are the inclination of the cone axis with respect to the line of sight (β) and the intrinsic outflow

velocity (v_{out}). With MOKA^{3D} we reproduce the line emission on a spaxel-by-spaxel basis, which as a consequence guarantee that the model reproduces the observed moment maps, with discrepancies between observed and modeled moment maps below 5%. We found that the best-fit parameters that reproduce the [Ne v] λ 14 μ m outflow features in NGC 1365 are $\beta = 82 \pm 6^\circ$, and $v_{\text{out}} = 390 \pm 35 \text{ km s}^{-1}$, consistent with the results in Marconcini et al. (2025b). Fig. 8 shows the 3D representation of this conical outflow. Moreover, we used MOKA^{3D} to fit the [O III] λ 5007 \AA spatially resolved emission assuming the same outflow geometry as for the [Ne v] λ 14 μ m emission and found $\beta = 84 \pm 5^\circ$, and $v_{\text{out}} = 470 \pm 40 \text{ km s}^{-1}$. These results are also valid in the region where we extracted the spectrum used for the HOMERUN fitting.

So, adopting $\Delta R = 252 \text{ pc}$ ($\sim 3''$, i.e. the sky-projected extension of the 1.5'' radius aperture), we obtain the results of the outflow energetics reported in Table 1. From HOMERUN, we calculate consistent mass outflow rates for [Ne v] λ 14 μ m and [O III] λ 5007 \AA , namely $\dot{M}_{[\text{NeV}]} = (1.72 \pm 0.20) \times 10^{-1} M_{\odot} \text{ yr}^{-1}$ and $\dot{M}_{[\text{OIII}]} = (1.68 \pm 0.31) \times 10^{-1} M_{\odot} \text{ yr}^{-1}$, respectively. Instead, with the classic approach the [O III]-derived outflow rate is two orders of magnitude larger than that from [Ne V]. This discrepancy is primarily driven by the underestimation of the [Ne v] outflow mass in the classical approach. Specifically, the classical [Ne v] outflow mass is ~ 75 times smaller than the [O III] estimate and ~ 40 times smaller than the HOMERUN value, while the classical [O III] mass is only a factor of ~ 2 higher than the HOMERUN mass. This asymmetric bias clearly demonstrates that the limitations of the standard method predominantly affects high-ionization tracers like [Ne V], leading to severely underestimated masses and consequently unreliable mass outflow rate calculations.

Our mass outflow rate estimate derived with MOKA^{3D} +HOMERUN models is about one order of magnitude larger than the total ionized outflow rate reported by Venturi et al. (2018), which was derived from the broad H α component in a shell-like region of the SE cone, extending from 1'' to 6'' from the nucleus. This large discrepancy clearly highlights how significantly the adopted methodology can affect the inferred outflow properties.

¹ The position angle is measured clockwise from North.

Table 1. Properties of the ionized outflow in NGC 1365 traced by [Ne v] λ 14 μ m and [O III] λ 5007 \AA emission lines.

Line	Method	M_{out} [$10^4 M_{\odot}$]	\dot{M}_{out} [$10^{-1} M_{\odot} \text{ yr}^{-1}$]	E_{out} [10^{53} erg]	\dot{E}_{out} [$10^{39} \text{ erg s}^{-1}$]
[Ne v] λ 14 μ m	standard	0.26 ± 0.10	0.041 ± 0.020	0.04 ± 0.02	0.20 ± 0.13
	HOMERUN	10.9 ± 0.2	1.7 ± 0.2	1.6 ± 0.3	8 ± 3
[O III] λ 5007 \AA	standard	20 ± 7	3.8 ± 0.18	4 ± 2	26 ± 17
	HOMERUN	8.8 ± 0.9	1.7 ± 0.3	1.9 ± 0.5	12 ± 4

Notes. From left to right: emission line, method used to compute the energetics, outflow velocity, mass outflow rate, kinetic energy, and power of the ionized outflow. These values are derived from the spatially resolved outflow properties in the FoV of MIRI Ch3, using the MOKA^{3D} tool.

4. Conclusions

In this work, we presented JWST/MIRI MRS observations of the active galaxy NGC 1365 as part of the Mid-IR Activity of Circumnuclear Line Emission (MIRACLE) program. We analyzed the spatially resolved gas properties and compared them with optical and mm observations from MUSE and ALMA, respectively. We traced both the ionized atomic and the warm and cold molecular gas phases in the circumnuclear region ($\sim 1.1 \times 1.0 \text{ kpc}^2$) of the NGC 1365 galaxy, identifying more than 40 mid-IR emission lines. Our main results are the following:

- We find that the mid-IR, optical, and mm emission lines consistently trace different phases of the gas with coherent internal kinematics within each phase (see Fig. 3 and Section 3.1). The cold molecular gas traced by the CO(3-2) transition shares the same ordered kinematics of the stellar galaxy disk (Venturi et al. 2018), with no evidence for outflowing material. The same conclusion holds for the warm molecular gas traced by the H₂ pure-rotational transitions, with the exception of a peculiar high- σ unresolved region located southwards of the nucleus.
- The ionized gas lines can be separated in two main groups which show opposed morphologies based on their ionization potential (IP). The high-IP ($>80 \text{ eV}$) emission lines trace the bipolar outflow, showing a velocity gradient perpendicular to the disk major axis, consistent with the [O III] λ 5007 \AA kinematics. The velocity dispersion map highlights a donut-shaped structure associated with the approaching side of the outflow which extends up to $2.5''$ ($\sim 200 \text{ pc}$). The low-IP ($<25 \text{ eV}$) emission line kinematics resembles the stellar galaxy disk ordered motions, similar to the H₂, with clumpy flux peaks in the circumnuclear star-forming ring. Finally, medium-IP lines show intermediate properties, with a kinematics similar to low-IP species but exhibiting the donut-shaped structure typical of the high-IP lines in the velocity dispersion map.
- [O III] λ 5007 \AA and [Ne v] λ 14 μ m velocity channel maps reveal that both outflowing species trace the same kinematic structures, with the [Ne v] λ 14 μ m appearing more collimated on the outflow axis, as expected from their different IPs (Fig. 4 and Section 3.2). The [Ne v] λ 14 μ m emission also reveals the NW receding counterpart of the ionization cone, which is undetected in [O III] λ 5007 \AA due to large extinction caused by the galaxy disk at optical wavelengths.
- The mid-IR emission-line ratios indicate a composite excitation scenario, with contribution from both AGN photoionization and shocks (Fig. 5 and Section 3.3). The AGN ionization seems to extend along the disk major axis, while in the other direction we observe shock-dominated zones, suggesting an

interaction between the outflow and the disk material. Notably, by penetrating the dust in the central regions of the galaxy, these mid-IR diagnostic diagrams reveal for the first time the role of the AGN in ionizing the gas in the nuclear region, differently from the optical diagnostic diagrams that mostly reveal excitation due to SF.

- The spatially resolved electron density map derived from the [Ne v] λ 24 μ m/[Ne v] λ 14 μ m line ratio shows a median density of $(750 \pm 440) \text{ cm}^{-3}$ (Fig. 6), ≈ 0.3 dex higher than the value inferred from optical [S II] λ 6716/[S II] λ 6731 line ratio (see Sections 3.4 and Appendix D).
- By exploiting the innovative photoionization modeling code HOMERUN, we derived the physical properties of the ionized outflowing gas, providing a self-consistent and physically motivated estimate of the outflow mass (Section 3.5). We obtain $M_{[\text{Ne v}]} = (109 \pm 2) \times 10^3 M_{\odot}$ and $M_{[\text{O III}]} = (88 \pm 9) \times 10^3 M_{\odot}$. These estimates differ significantly from those derived with the standard method, which are ~ 40 times lower ([Ne v]) and ~ 2 times higher ([O III]) than those obtained from HOMERUN. This discrepancy reflects the strong assumptions in the classical approach regarding ionization state, average density, and extinction correction.
- We find a consistent outflow mass rate of $\sim 0.17 M_{\odot} \text{ yr}^{-1}$ from [Ne v] λ 14 μ m and [O III] λ 5007 \AA (Section 3.6). Our estimate is about one order of magnitude higher than the value reported in the literature, clearly illustrating how different methods can significantly impact the inferred outflow properties. To derive the intrinsic outflow velocities, we used the 3D MOKA^{3D} kinematic model, assuming a conical geometry. The best-fit solutions provide consistent inclination angles ($\beta \sim 82\text{-}84^\circ$) and outflow velocities ($v_{\text{out}} \sim 390\text{-}470 \text{ km s}^{-1}$) for both [Ne v] λ 14 μ m and [O III] λ 5007 \AA , reinforcing the reliability of our kinematic and energetic estimates.

This work highlights the critical need for self-consistent, multi-line photoionization and kinematical modeling to properly capture the complex structure and energetics of AGN-driven outflows - a key step toward understanding their impact on galaxy evolution. We fully exploited the synergy between cutting-edge IFU facilities, JWST/MIRI and VLT/MUSE, to model the ionized gas phase properties across a broad ionization range (from $\sim 10 \text{ eV}$ to $\sim 130 \text{ eV}$), using a total of 60 emission lines. For the first time, we combined detailed 3D kinematic modeling with MOKA^{3D} and photoionization fitting with HOMERUN to derive the intrinsic structure and physical conditions of the outflow in a fully self-consistent framework. This unprecedented approach enabled a coherent and physically motivated characterization of the outflow's spatial structure, ionization stratification, and ener-

getics. Our results show that classical methods, based on simplified assumptions and a limited set of tracers, significantly underestimate the outflow energetics - and hence the strength of AGN feedback.

Acknowledgements. We are grateful to S. Charlot for kindly providing the predictions for the SF line-emission models. EB, FB, and GC acknowledge financial support from INAF under the Large Grant 2022 “The metal circle: a new sharp view of the baryon cycle up to Cosmic Dawn with the latest generation IFU facilities” and the GO grant 2024 “A JWST/MIRI MIRACLE: Mid-IR Activity of Circumnuclear Line Emission”. IL, FB, and AM acknowledge support from PRIN-MUR project “PROMETEUS” financed by the European Union - Next Generation EU, Mission 4 Component 1 CUP B53D23004750006. EB acknowledges INAF funding through the “Ricerca Fondamentale 2024” program (mini-grant 1.05.24.07.01). IL and AM acknowledges support from PRIN-MUR project “PROMETEUS” financed by the European Union - Next Generation EU, Mission 4 Component 1 CUP B53D23004750006. AM, MG, IL and CM acknowledge INAF funding through the “Ricerca Fondamentale 2023” program (mini-grant 1.05.23.04.01). FS acknowledges financial support from the PRIN MUR 2022 2022TKPB2P - BIG-z, Ricerca Fondamentale INAF 2023 Data Analysis grant 1.05.23.03.04 “ARCHIE ARchive Cosmic HI & ISM Evolution”, Ricerca Fondamentale INAF 2024 under project 1.05.24.07.01 MINI-GRANTS RSN1 “ECHOS”. Bando Finanziamento ASI CI-UCO-DSR-2022-43 project “IBISCO: feedback and obscuration in local AGN”. GS acknowledges the project PRIN-MUR 2020 MUR BEYOND-2p (“Astrochemistry beyond the second period elements”, Prot. 2020AFB3FX), the PRIN MUR 2022 FOSSILS (“Chemical origins: linking the fossil composition of the Solar System with the chemistry of protoplanetary disks”, Prot. 2022JC2Y93), the project ASI-Astrobiologia 2023 MIGLIORA (“Modeling Chemical Complexity”, F83C23000800005), the INAF-GO 2023 fundings PROTOSKA (“Exploiting ALMA data to study planet forming disks: preparing the advent of SKA”, C13C23000770005) and the INAF-Minigrant 2023 TRIESTE (“Tracing the chemical heritage of our origin: from proTostars to planEts”; PI: G. Sabatini). SC and GV acknowledge support by European Union’s HE ERC Starting Grant No. 101040227 - WINGS. JF acknowledges financial support from CONAH-CyT, project number CF-2023-G100, and UNAM-DGAPA-PAPIIT IN111620 grant, Mexico. AVG acknowledges support from the Spanish grant PID2022-138560NB-I00, funded by MCIN/AEI/10.13039/501100011033/FEDER, EU. MM is thankful for support from the European Space Agency (ESA). EH gratefully acknowledges the hospitality of the IAC, where part of this work was carried out during a long research visit. This work is based on observations made with the NASA/ESA/CSA James Webb Space Telescope. The data were obtained from the Mikulski Archive for Space Telescopes at the Space Telescope Science Institute, which is operated by the Association of Universities for Research in Astronomy, Inc., under NASA contract NAS 5-03127 for JWST. The specific observations analyzed can be accessed via doi: <https://doi.org/10.17909/b4w1-hk44>. These observations are associated with program #6138. The authors acknowledge the team led by coPIs C. Marconcini and A. Feltre for developing their observing program with a zero-exclusive-access period. This paper makes use of the following ALMA data: ADS/JAO.ALMA#2016.1.00296.S. ALMA is a partnership of ESO (representing its member states), NSF (USA) and NINS (Japan), together with NRC (Canada), NSTC and ASIAA (Taiwan), and KASI (Republic of Korea), in cooperation with the Republic of Chile. The Joint ALMA Observatory is operated by ESO, AUI/NRAO and NAOJ.

References

Alarie, A. & Morisset, C. 2019, *Rev. Mexicana Astron. Astrofis.*, 55, 377
 Alonso-Herrero, A., Sánchez-Portal, M., Ramos Almeida, C., et al. 2012, *MNRAS*, 425, 311
 Anand, G. S., Lee, J. C., Van Dyk, S. D., et al. 2021, *MNRAS*, 501, 3621
 Argyriou, I., Glasse, A., Law, D. R., et al. 2023, *A&A*, 675, A111
 Argyriou, I., Wells, M., Glasse, A., et al. 2020, *A&A*, 641, A150
 Asplund, M., Amarsi, A. M., & Grevesse, N. 2021, *A&A*, 653, A141
 Asplund, M., Grevesse, N., Sauval, A. J., & Scott, P. 2009, *ARA&A*, 47, 481
 Audibert, A., Ramos Almeida, C., García-Burillo, S., et al. 2023, *A&A*, 671, L12
 Bacon, R., Accardo, M., Adjali, L., et al. 2010, in *Society of Photo-Optical Instrumentation Engineers (SPIE) Conference Series*, Vol. 7735, *Ground-based and Airborne Instrumentation for Astronomy III*, ed. I. S. McLean, S. K. Ramsay, & H. Takami, 773508
 Baldwin, J. A., Phillips, M. M., & Terlevich, R. 1981, *PASP*, 93, 5
 Belli, S., Park, M., Davies, R. L., et al. 2024, *Nature*, 630, 54
 Boroson, T. A. & Green, R. F. 1992, *ApJS*, 80, 109
 Braito, V., Reeves, J. N., Gofford, J., et al. 2014, *ApJ*, 795, 87
 Bureau, M., Mould, J. R., & Staveley-Smith, L. 1996, *ApJ*, 463, 60

Bushouse, H., Eisenhamer, J., Dencheva, N., et al. 2022, *spacetelescope/jwst: JWST* 1.6.2
 Byrne, C. M., Stanway, E. R., Eldridge, J. J., McSwiney, L., & Townsend, O. T. 2022, *MNRAS*, 512, 5329
 Cano-Díaz, M., Maiolino, R., Marconi, A., et al. 2012, *A&A*, 537, L8
 Cappellari, M. & Copin, Y. 2003, *MNRAS*, 342, 345
 Cappellari, M. & Emsellem, E. 2004, *PASP*, 116, 138
 Carniani, S., Marconi, A., Maiolino, R., et al. 2015, *A&A*, 580, A102
 CASA Team, Bean, B., Bhatnagar, S., et al. 2022, *PASP*, 134, 114501
 Ceci, M., Cresci, G., Arribas, S., et al. 2025, *A&A*, 695, A116
 Ciccone, C., Brusa, M., Ramos Almeida, C., et al. 2018, *Nature Astronomy*, 2, 176
 Combes, F. 2017, *Frontiers in Astronomy and Space Sciences*, 4, 10
 Combes, F., García-Burillo, S., Audibert, A., et al. 2019, *A&A*, 623, A79
 Cresci, G. & Maiolino, R. 2018, *Nature Astronomy*, 2, 179
 Cresci, G., Marconi, A., Zibetti, S., et al. 2015, *A&A*, 582, A63
 Cresci, G., Tozzi, G., Perna, M., et al. 2023, *A&A*, 672, A128
 Davies, R., Shimizu, T., Pereira-Santaella, M., et al. 2024, *A&A*, 689, A263
 de Vaucouleurs, G., de Vaucouleurs, A., Corwin, Jr., H. G., et al. 1991, *Third Reference Catalogue of Bright Galaxies*
 Dopita, M. A., Fischera, J., Sutherland, R. S., et al. 2006, *ApJS*, 167, 177
 Dudik, R. P., Weingartner, J. C., Satyapal, S., et al. 2007, *ApJ*, 664, 71
 Fabian, A. C. 2012, *ARA&A*, 50, 455
 Feltre, A., Gruppioni, C., Marchetti, L., et al. 2023, *A&A*, 675, A74
 Ferland, G. J., Korista, K. T., Verner, D. A., et al. 1998, *PASP*, 110, 761
 Feruglio, C., Maiolino, R., Piconcelli, E., et al. 2010, *A&A*, 518, L155
 Fiore, F., Feruglio, C., Shankar, F., et al. 2017, *A&A*, 601, A143
 Fluetsch, A., Maiolino, R., Carniani, S., et al. 2021, *MNRAS*, 505, 5753
 Fluetsch, A., Maiolino, R., Carniani, S., et al. 2019, *MNRAS*, 483, 4586
 Forbes, D. A. & Norris, R. P. 1998, *MNRAS*, 300, 757
 Förster Schreiber, N. M., Übler, H., Davies, R. L., et al. 2019, *ApJ*, 875, 21
 Gao, Y., Egusa, F., Liu, G., et al. 2021, *ApJ*, 913, 139
 García-Berete, I., Alonso-Herrero, A., Rigopoulou, D., et al. 2024, *A&A*, 681, L7
 García-Burillo, S., Combes, F., Ramos Almeida, C., et al. 2019, *A&A*, 632, A61
 Garofali, K., Basu-Zych, A. R., Johnson, B. D., et al. 2024, *ApJ*, 960, 13
 Gordon, K. D., Clayton, G. C., Declair, M., et al. 2023, *ApJ*, 950, 86
 Groves, B. A., Dopita, M. A., & Sutherland, R. S. 2004, *ApJS*, 153, 75
 Gutkin, J., Charlot, S., & Bruzual, G. 2016, *MNRAS*, 462, 1757
 Hao, L., Wu, Y., Charmandaris, V., et al. 2009, *ApJ*, 704, 1159
 Harrison, C. M., Alexander, D. M., Mullaney, J. R., et al. 2016, *MNRAS*, 456, 1195
 Harrison, C. M., Alexander, D. M., Mullaney, J. R., & Swinbank, A. M. 2014, *MNRAS*, 441, 3306
 Harrison, C. M. & Ramos Almeida, C. 2024, *Galaxies*, 12, 17
 Hatziminaoglou, E., Zwaan, M., Andreani, P., et al. 2015, *The Messenger*, 162, 24
 Hermosa Muñoz, L., Alonso-Herrero, A., Labiano, A., et al. 2024a, *arXiv e-prints*, arXiv:2412.14707
 Hermosa Muñoz, L., Alonso-Herrero, A., Labiano, A., et al. 2024b, *arXiv e-prints*, arXiv:2412.14707
 Hill, M. J. & Zakamska, N. L. 2014, *MNRAS*, 439, 2701
 Inami, H., Armus, L., Charmandaris, V., et al. 2013, *ApJ*, 777, 156
 Jones, J. E. & Jones, B. J. T. 1980, *MNRAS*, 191, 685
 Kakkad, D., Groves, B., Dopita, M., et al. 2018, *A&A*, 618, A6
 Kakkad, D., Mainieri, V., Vietri, G., et al. 2020, *A&A*, 642, A147
 Kewley, L. J., Dopita, M. A., Sutherland, R. S., Heisler, C. A., & Trevena, J. 2001, *ApJ*, 556, 121
 Kewley, L. J., Groves, B., Kauffmann, G., & Heckman, T. 2006, *MNRAS*, 372, 961
 Kewley, L. J., Maier, C., Yabe, K., et al. 2013, *ApJ*, 774, L10
 Kristen, H., Jorsater, S., Lindblad, P. O., & Bokserberg, A. 1997, *A&A*, 328, 483
 Kroupa, P. 2001, *MNRAS*, 322, 231
 Labiano, A., Argyriou, I., Álvarez-Márquez, J., et al. 2021, *A&A*, 656, A57
 Law, D. R., E. Morrison, J., Argyriou, I., et al. 2023, *AJ*, 166, 45
 Lee, J. C., Sandstrom, K. M., Leroy, A. K., et al. 2023, *ApJ*, 944, L17
 Lee, J. C., Whitmore, B. C., Thilker, D. A., et al. 2022, *ApJS*, 258, 10
 Lindblad, P. O., Hjelm, M., Hoegbom, J., et al. 1996, *A&AS*, 120, 403
 Liu, D., Schinnerer, E., Cao, Y., et al. 2023, *ApJ*, 944, L19
 Luridiana, V., Morisset, C., & Shaw, R. A. 2015, *A&A*, 573, A42
 Lutz, D., Sturm, E., Janssen, A., et al. 2020, *A&A*, 633, A134
 Marasco, A., Cresci, G., Nardini, E., et al. 2020, *A&A*, 644, A15
 Marconcini, C., Feltre, A., Lamperti, I., et al. 2025a, *arXiv e-prints*, arXiv:2503.21921
 Marconcini, C., Marconi, A., Cresci, G., et al. 2025b, *Nature Astronomy* [arXiv:2503.24359]
 Marconcini, C., Marconi, A., Cresci, G., et al. 2023, *A&A*, 677, A58
 Marconi, A., Amiri, A., Feltre, A., et al. 2024, *A&A*, 689, A78
 Martínez-Paredes, M., Bruzual, G., Morisset, C., et al. 2023, *MNRAS*, 525, 2916

- Mingozzi, M., Cresci, G., Venturi, G., et al. 2019, *A&A*, 622, A146
- Mingozzi, M., Garcia del Valle-Espinosa, M., James, B. L., et al. 2025, *ApJ*, 985, 253
- Morrison, J. E., Dicken, D., Argyriou, I., et al. 2023, *PASP*, 135, 075004
- Mulcahey, C. R., Leslie, S. K., Jackson, T. M., et al. 2022, *A&A*, 665, A144
- Nicholls, D. C., Sutherland, R. S., Dopita, M. A., Kewley, L. J., & Groves, B. A. 2017, *MNRAS*, 466, 4403
- Osterbrock, D. E. & Ferland, G. J. 2006, *Astrophysics of gaseous nebulae and active galactic nuclei*
- Patapis, P., Argyriou, I., Law, D. R., et al. 2024, *A&A*, 682, A53
- Perna, M., Arribas, S., Lamperti, I., et al. 2024, *A&A*, 690, A171
- Perrin, M. D., Sivaramakrishnan, A., Lajoie, C.-P., et al. 2014, in *Society of Photo-Optical Instrumentation Engineers (SPIE) Conference Series*, Vol. 9143, *Space Telescopes and Instrumentation 2014: Optical, Infrared, and Millimeter Wave*, ed. J. M. Oschmann, Jr., M. Clampin, G. G. Fazio, & H. A. MacEwen, 91433X
- Ramos Almeida, C., Bischetti, M., García-Burillo, S., et al. 2022, *A&A*, 658, A155
- Ramos Almeida, C., Garcia-Bernete, I., Pereira-Santaella, M., et al. 2025, arXiv e-prints, arXiv:2504.01595
- Richardson, C. T., Simpson, C., Polimera, M. S., et al. 2022, *ApJ*, 927, 165
- Richings, A. J. & Faucher-Giguère, C.-A. 2018a, *MNRAS*, 478, 3100
- Richings, A. J. & Faucher-Giguère, C.-A. 2018b, *MNRAS*, 474, 3673
- Rieke, G. H., Wright, G. S., Böker, T., et al. 2015, *PASP*, 127, 584
- Riffel, R. A., Zakamska, N. L., & Riffel, R. 2020, *MNRAS*, 491, 1518
- Risaliti, G., Bianchi, S., Matt, G., et al. 2005, *ApJ*, 630, L129
- Sakamoto, K., Ho, P. T. P., Mao, R.-Q., Matsushita, S., & Peck, A. B. 2007, *ApJ*, 654, 782
- Sanchez, R. Z. 2009, PhD thesis, Rutgers University, New Jersey
- Sandqvist, A., Joersaeter, S., & Lindblad, P. O. 1995, *A&A*, 295, 585
- Schinnerer, E., Emsellem, E., Henshaw, J. D., et al. 2023, *ApJ*, 944, L15
- Sharp, R. G. & Bland-Hawthorn, J. 2010, *ApJ*, 711, 818
- Speranza, G., Ramos Almeida, C., Acosta-Pulido, J. A., et al. 2024, *A&A*, 681, A63
- Stanway, E. R. & Eldridge, J. J. 2018, *MNRAS*, 479, 75
- Stevens, I. R., Forbes, D. A., & Norris, R. P. 1999, *MNRAS*, 306, 479
- Teuben, P. J., Sanders, R. H., Atherton, P. D., & van Albada, G. D. 1986, *MNRAS*, 221, 1
- Tozzi, G., Cresci, G., Marasco, A., et al. 2021, *A&A*, 648, A99
- Ulivi, L., Perna, M., Lamperti, I., et al. 2025, *A&A*, 693, A36
- Vazdekis, A., Koleva, M., Ricciardelli, E., Röck, B., & Falcón-Barroso, J. 2016, *MNRAS*, 463, 3409
- Veilleux, S., Cecil, G., & Bland-Hawthorn, J. 2005, *ARA&A*, 43, 769
- Veilleux, S. & Osterbrock, D. E. 1987, *ApJS*, 63, 295
- Venturi, G., Cresci, G., Marconi, A., et al. 2021, *A&A*, 648, A17
- Venturi, G., Marconi, A., Mingozzi, M., et al. 2017, *Frontiers in Astronomy and Space Sciences*, 4, 46
- Venturi, G., Nardini, E., Marconi, A., et al. 2018, *A&A*, 619, A74
- Venturi, G., Treister, E., Finlez, C., et al. 2023, *A&A*, 678, A127
- Véron-Cetty, M. P. & Véron, P. 2006, *A&A*, 455, 773
- Weaver, K. A., Meléndez, M., Mushotzky, R. F., et al. 2010, *ApJ*, 716, 1151
- Woo, J.-H., Bae, H.-J., Son, D., & Karouzos, M. 2016, *ApJ*, 817, 108
- Wooten, A. & Thompson, A. R. 2009, *IEEE Proceedings*, 97, 1463
- Wright, G. S., Rieke, G. H., Glasse, A., et al. 2023, *PASP*, 135, 048003
- Zhang, L., Packham, C., Hicks, E. K. S., et al. 2024, *ApJ*, 974, 195
- Zubovas, K. & Bourne, M. A. 2017, *MNRAS*, 468, 4956

Appendix A: Observations and data reduction

In this appendix, we present the observations and data reduction for MIRI MRS, MUSE, and ALMA data.

Appendix A.1: JWST/MIRI

We refer to [Marconcini et al. \(2025a\)](#) for a detailed description of the different steps performed during the data reduction and briefly summarize them here. We downloaded the uncalibrated science and background observations through the Barbara A. Mikulski Archive for Space Telescopes (MAST) portal². The data reduction process was performed using the JWST Science Calibration Pipeline ([Bushouse et al. 2022](#)) version 1.16.0 with JWST Calibration Reference Data System context file 1298. We applied all three stages of the pipeline processing, which include CALWEBB_DETECTOR1, CALWEBB_SPEC2, and CALWEBB_SPEC3 (see [Argyriou et al. 2020, 2023; Morrison et al. 2023; Patapis et al. 2024](#)). For NGC 1365, we subtracted the background emission from the 2D science images using a background frame generated from our dedicated background observations. Moreover, we performed two residual fringe corrections, both in stage 2 and 3. Additionally, to improve the final datacubes, we adopted the Exponential Modified-Shepard Method (EMSM) weighting function, which has proven to be more efficient in reducing the drizzling effect ([Law et al. 2023](#)).

Finally, we applied an astrometric correction to all the datacubes with different ΔRA and ΔDec for each band, using the ALMA astrometry as reference (details in Appendix B).

Appendix A.2: MUSE Wide Field Mode

The data were retrieved from the ESO archive³ and were already processed automatically using the standard MUSE pipeline (v1.6), with an average PSF FWHM of $0.8''$. The final datacube covers a FoV of $64'' \times 63.4''$, with a pixel size of $0.2''$ pixel⁻¹. The MUSE FoV covers approximately the central 5.3×5.3 kpc² of NGC 1365. MUSE resolving power in Wide Field Mode (WFM) varies from $R \sim 1770$ at 4800 \AA to 3590 at 9300 \AA . Finally, we apply a relative astrometric correction, registering the position of the continuum peak, measured in the line-free $7660\text{-}8000 \text{ \AA}$ wavelength range, to the nucleus position from the ALMA data (see Appendix A.3), as done for JWST/MIRI data (see Appendix A.1). The applied corrections were ΔRA and ΔDec shifts of $(-0.78'', +0.22'')$.

The MUSE integrated spectra of NGC 1365 extracted from the $0.7''$ radius regions shown in the lower-left panel of Fig. 1 are reported in Fig. A.1. The green (blue) spectrum is extracted from a region where the outflow (stellar disk) emission is predominant. We detect approximately 30 emission lines (see Table F.1) tracing different gas phases, including recombination lines, atomic lines, and lines from ionized gas.

Appendix A.3: ALMA

The data include observations with two different configurations with angular resolutions in FWHM of $\sim 0.30''$ and $\sim 0.07''$, respectively. In this work, we use the observations with resolution $\sim 0.30''$ corresponding to 30 pc, which better match the MIRI MRS spatial resolution and provide a maximum recoverable scale of $2.9''$. We retrieved the calibrated measurement sets

using the dedicated service provided by the European ALMA Regional Center ([Hatziminaoglou et al. 2015](#)). Imaging was performed using the Common Astronomy Software Applications (CASA) v6.1.1 ([CASA Team et al. 2022](#)). For the CO(3–2) spectral window (342.99 – 344.86 GHz), we subtracted a constant continuum level estimated from the emission line-free channels in the uv plane. The data were cleaned using the `tclean` task in CASA, with briggs weighting scheme with a robust parameter of 0.5, which resulted in a beam with a FWHM of $0.35'' \times 0.31''$ (beam PA = -71°), corresponding to ~ 37 pc in physical scale. The final datacube has a spectral channel width of $\sim 8 \text{ km s}^{-1}$, a pixel size of $0.05''$, a FoV of $25''$ in diameter and rms of $1.5 \text{ mJy beam}^{-1}$ per channel.

Finally, we fit the central $2'' \times 2''$ of the CO(3-2) flux map (see Appendix C.3) with a Gaussian profile to determine the coordinates of the nucleus, taking advantage of the high astrometric accuracy provided by ALMA. We find the nuclear position to be RA = 03h33m36.37s and Dec = -36d08m25.37s, in good agreement with the values reported by [Liu et al. \(2023\)](#). These coordinates are adopted throughout the rest of the paper and used to register the astrometry of MIRI and MUSE observations (see Appendices A.1 and A.2, respectively).

Appendix B: MIRI datacubes corrections

For the astrometric registration of the 12 datacubes, we applied separate corrections for each band (SHORT, MEDIUM, and LONG), as each observing setup corresponds to a different grating configuration of the MRS. As discussed in Appendix A.1, the observations are centered on the SE outflow cone rather than the AGN. This positioning causes the source to fall near the edge, or even slightly outside, of the field of view in the Ch1 datacubes (see Fig. 1). To ensure accurate alignment across the dataset, we computed the astrometric corrections using Ch3, where the source is well within the FoV and the spatial resolution remains high, providing a reliable reference frame for registration. We collapsed the datacubes along the spectral dimension and fitted the PSFs with a 2D Gaussian model. Then, we aligned the datacubes to match the PSF peaks with the AGN coordinates provided ALMA data (see Appendix A.3). The applied corrections were ΔRA and ΔDec shifts of $(+0.0086'', -0.2655'')$, $(+0.0256'', -0.2713'')$, and $(-0.0300'', -0.299'')$ for the SHORT, MEDIUM, and LONG channels, respectively.

To compare flux maps of emission lines from different channels it is crucial to account for the different pixel size (see Appendix A.1). To address this, we rebinned each channel to match the pixel size of Ch4, which has the worst resolution ($0.35''$). We used the `reproject_exact` function to ensure flux conservation during the resampling process. In Fig. B.1 we show the collapsed datacubes before and after the spatial rebinning. The relative flux conservation error is below the 1%, so negligible respect the original flux.

MIRI data are known to exhibit flux discontinuities between different sub-channels. This effect could be amplified after the rebinning for the different pixel size of data. Therefore, it is essential to apply a scaling factor to the fluxes when constructing a single spectrum, in addition to account for differences in spectral sampling. To address this, we implemented a stitching procedure between each pair of datacubes by rescaling the flux of the bluer datacube to match the median flux value of the overlapping spectral channels of the redder datacube. We chose to rescale to the reddest datacube (Ch4 LONG) as it has the largest FoV, ensuring consistent scaling in every spaxel. This process yielded a scaling factor matrix for each pair of datacubes, which was then applied

² <https://www.vla.nrao.edu/astro/nvas/avla.shtml>

³ <https://archive.eso.org/cms.html>

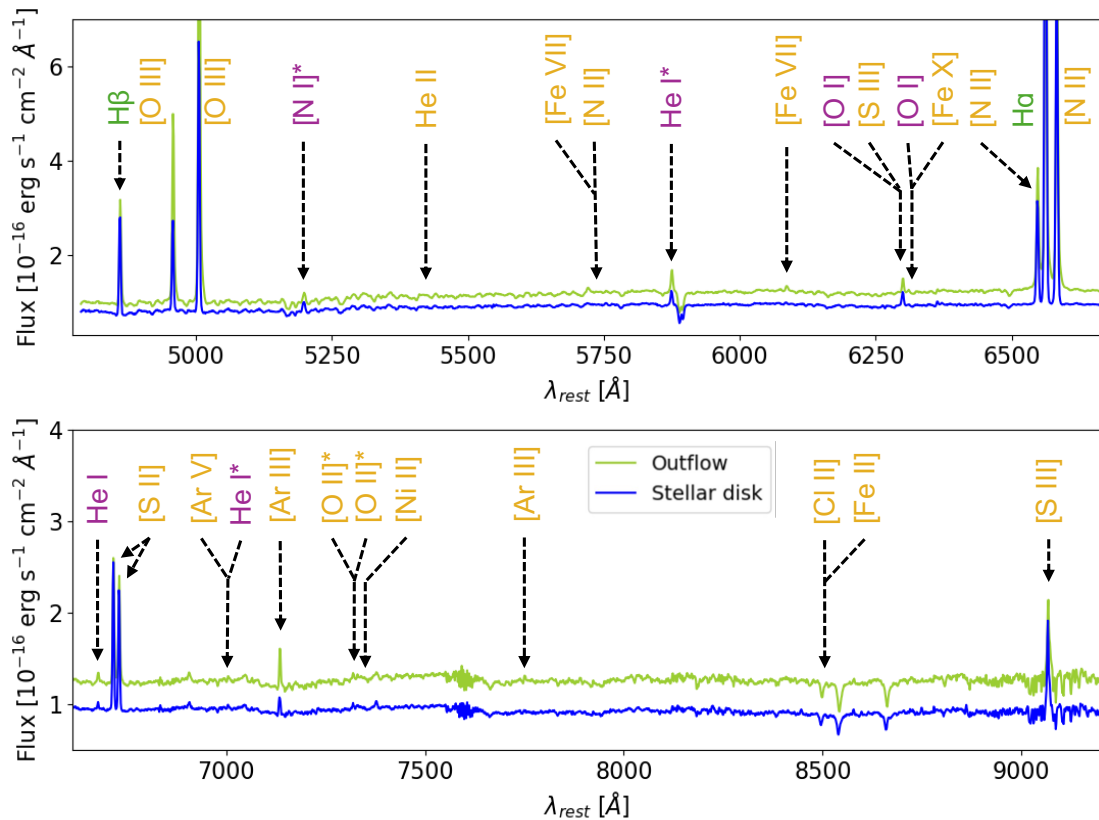


Fig. A.1. Integrated spectra of NGC 1365 from MUSE data. The blue and green curves represent the integrated spectra extracted with a $0.7''$ radius aperture from regions dominated by the stellar disk and outflow emission, respectively (see Fig. 1, lower right panel). Detected emission lines are marked with vertical lines: ionized gas emission lines in yellow, atomic lines in violet, and H I recombination lines in green. An asterisk indicates species corresponding to blends of two or three emission lines.

to correct all fluxes derived from our data. In Fig. B.2 an example of the total spectrum before and after the stitching procedure.

As shown in Law et al. (2023), the average FWHM of the MIRI/MRS PSF varies across the four channels spanning the range $\text{FWHM} = 0.4'', 0.5'', 0.6'', 0.9''$, in Ch1, Ch2, Ch3, Ch4, respectively. This variation must be taken into account when computing ratios between emission lines at different wavelengths. To ensure consistent spatial resolution, we firstly downloaded the MIRI MRS PSF model cube using the *WebbPSF* tool v.1.4.0 (Perrin et al. 2014), which provide a model cube spatially oversampled of a factor of 4 with respect to the observations (i.e. $0.05''/\text{pixel}$ for Ch3). Then we deconvolved each flux map with the PSF corresponding to the wavelength of the emission line, and convolved it with the PSF at the reddest wavelength among the lines involved in the ratios, using the PSF model cubes from *WebbPSF*. The deconvolution procedure is composed by a wavelength-dependent alignment, rotation and flux normalization between the PSFs and our flux maps, following a similar methodology of Marconcini et al. (2025a).

Appendix C: Data analysis

In this appendix, we describe the general methodology employed for the emission line analysis of data from MUSE, ALMA, and MIRI MRS. In particular, we analyzed the MUSE and MIRI data to subtract the continuum and fit the emission lines in the optical and the mid-IR band, using a multi-Gaussian fitting procedure.

Appendix C.1: JWST/MIRI MRS emission line fitting

This appendix provides further details on the customized python routine we employed to analyze the MIRI MRS datacubes. We followed a three-step procedure: first, we applied spatial smoothing to enhance the SNR; second, we subtracted the local continuum around the brightest emission lines; finally, we performed spaxel-by-spaxel Gaussian fitting of the residual emission. First, we applied a Gaussian spatial smoothing with a kernel size of 1 pixel to every spatial plane of the datacube. This step improves the SNR of faint extended features, at the cost of a moderate degradation in spatial resolution. Specifically, the effective PSF is broadened by approximately 40% across all wavelengths, due to the fact that the pixel size is comparable to or slightly smaller than the intrinsic PSF σ at each wavelength. Nevertheless, the resulting resolution remains sufficient for our spatially resolved analysis, as it still allows us to distinguish the relevant morphological and kinematic structures in the data.

We then performed the emission line fitting spaxel-by-spaxel, fitting each line in Table C.1 independently. Prior to this, we modeled and fitted the local continuum selecting wavelength windows on either side of the line, adjusting the range based on the FWHM of each emission line and carefully avoiding other spectral absorption or emission features. Given the short spectral window of $\sim 0.1 \mu\text{m}$ we considered, within which the continuum is featureless, we fitted the continuum with a straight line. Each emission line is modeled with both a single and a double Gaussian component, and then we applied a Kolmogorov-Smirnov (KS) test on the residuals to choose the optimal number of Gaussian components in each spaxel, adopting a threshold p-value of

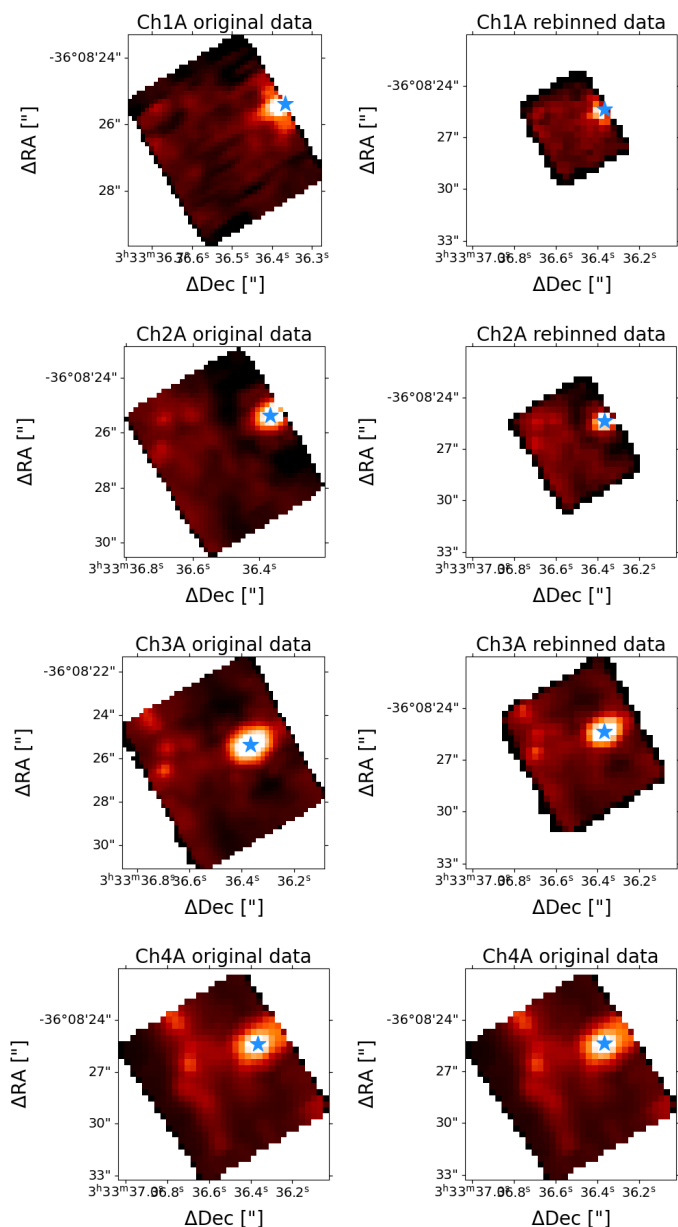


Fig. B.1. Examples of the rebinning procedure for datacubes in the A (SHORT) band. Left column shows the original collapsed data with native pixel size and original FoVs. Right column shows the same data after the rebinning, sharing the wider FoV (i.e. Ch4). The star marks the nucleus position.

0.7 (see [Marasco et al. 2020](#); [Tozzi et al. 2021](#); [Ceci et al. 2025](#) for details).

In the mid-IR, dust attenuation is much lower than at optical wavelengths, but it does vary with wavelength and affect emission lines differently, potentially impacting specific line ratios. Unfortunately, in our data the SNR of the $\text{Pf}\alpha$ and $\text{Hu}\alpha$ (i.e. H I (6-5) at $7.46 \mu\text{m}$ and H I (7-6) at $12.37 \mu\text{m}$, respectively) is too low to derive a reliable extinction map directly from the mid-IR spectra. To test the potential impact of dust attenuation, we applied an extinction correction to the mid-IR emission lines using the [Gordon et al. \(2023\)](#) attenuation curve and adopting the maximum A_V value (~ 3) derived from our best-fit photoionization model (see Section 3.5.3). However, we find that the resulting variations in the mid-IR line ratios are within the errors,

Table C.1. List of the fitted emission lines in the MIRI spectra

Emission line	$\lambda^{(1)}$ [μm]	IP ⁽¹⁾ [eV]	Ch	Flux [$10^{-14} \text{ erg s}^{-1} \text{ cm}^{-2}$]
[Mg v]	5.61	109	1A	1.75 ± 0.05
$\text{Pf}\alpha$	7.46	-	1C	0.962 ± 0.005
[Ne vi]	7.65	126	2A	8.44 ± 0.09
[Ar v]	7.90	60	2A	1.4 ± 0.1
H ₂ 0-0 S(4)	8.03	-	2A	2.06 ± 0.04
[Ar iii]	8.99	28	2B	3.4 ± 0.2
H ₂ 0-0 S(3)	9.66	-	2B	4.6 ± 0.6
[S iv]	10.51	35	2C	24.0 ± 0.4
H ₂ 0-0 S(2)	12.28	-	3A	7.5 ± 0.1
$\text{Hu}\alpha$	12.37	-	3A	0.760 ± 0.002
[Ne ii]	12.81	23	3A	102.6 ± 0.4
[Ar v]	13.10	60	3A	0.702 ± 0.004
[Ne v]	14.32	97	3B	22.2 ± 0.4
[Cl ii]	14.37	13	3B	2.02 ± 0.03
[Ne iii]	15.56	41	3C	56.6 ± 0.4
H ₂ 0-0 S(1)	17.04	-	3C	16.3 ± 0.4
[S iii]	18.71	23	4A	50.5 ± 0.2
[Ne v]	24.32	97	4C	26.70 ± 0.04
[O iv]	25.89	55	4C	53.0 ± 2.0

Notes. From left to right: the name of the emission line, the corresponding wavelength, the ionization potential (defined as the energy required to create the observed transition), the MIRI channel it belongs to, and the integrated observed flux in the FoV of the respective channel, expressed in units of $10^{-14} \text{ erg s}^{-1} \text{ cm}^{-2}$.

References. (1) [ISO Spectrometer Data Centre](#).

including those involving emission lines at distant wavelengths (e.g., $[\text{Ne v}]\lambda 24 \mu\text{m}/[\text{Ne v}]\lambda 14 \mu\text{m}$, see Section 3.4).

Appendix C.2: MUSE WFM emission line fitting

MUSE data were analyzed as already described in previous works of the MAGNUM program ([Venturi et al. 2018](#); [Mingozzi et al. 2019](#)). Briefly, after a preliminary Voronoi tessellation ([Cappellari & Copin 2003](#)) to achieve an average SNR per wavelength channel of at least 70 on the continuum, we applied the penalized PiXel-Fitting (pPXF, [Cappellari & Emsellem 2004](#)) code to measure the optical emission lines listed in Table F.1. Using the penalized PiXel-Fitting (pPXF, [Cappellari & Emsellem 2004](#)) code, we fitted simultaneously the continuum and gas emission in the wavelength range $4800\text{-}9200 \text{ \AA}$, convolving a linear combination of stellar templates (E-MILES; for details see [Vazdekis et al. 2016](#)) with a Gaussian velocity distribution. Each emission line was fitted twice, using one and two Gaussian components, and the KS test was applied spaxel-by-spaxel to determine the minimum number of components required to adequately reproduce the line profiles (see Appendix C.1). Given that NGC 1365 hosts a Seyfert 1.8 nucleus, we included an additional spectral component when fitting the bins within a radius of 10 spaxels from the nuclear position to account for the spatially unresolved broad-line region (BLR). The BLR model consists of two independent components: a broad ($\sigma > 1000 \text{ km s}^{-1}$) Gaussian component for the broad Balmer lines (i.e. $\text{H}\alpha$ and $\text{H}\beta$) and a template of broad $[\text{Fe II}]$ emission features by [Boroson & Green \(1992\). The nuclear model spectrum was obtained by fitting the integrated spectrum of the central spaxels and, in the subsequent spaxel-by-spaxel fitting, it was kept fixed in shape and velocity](#)

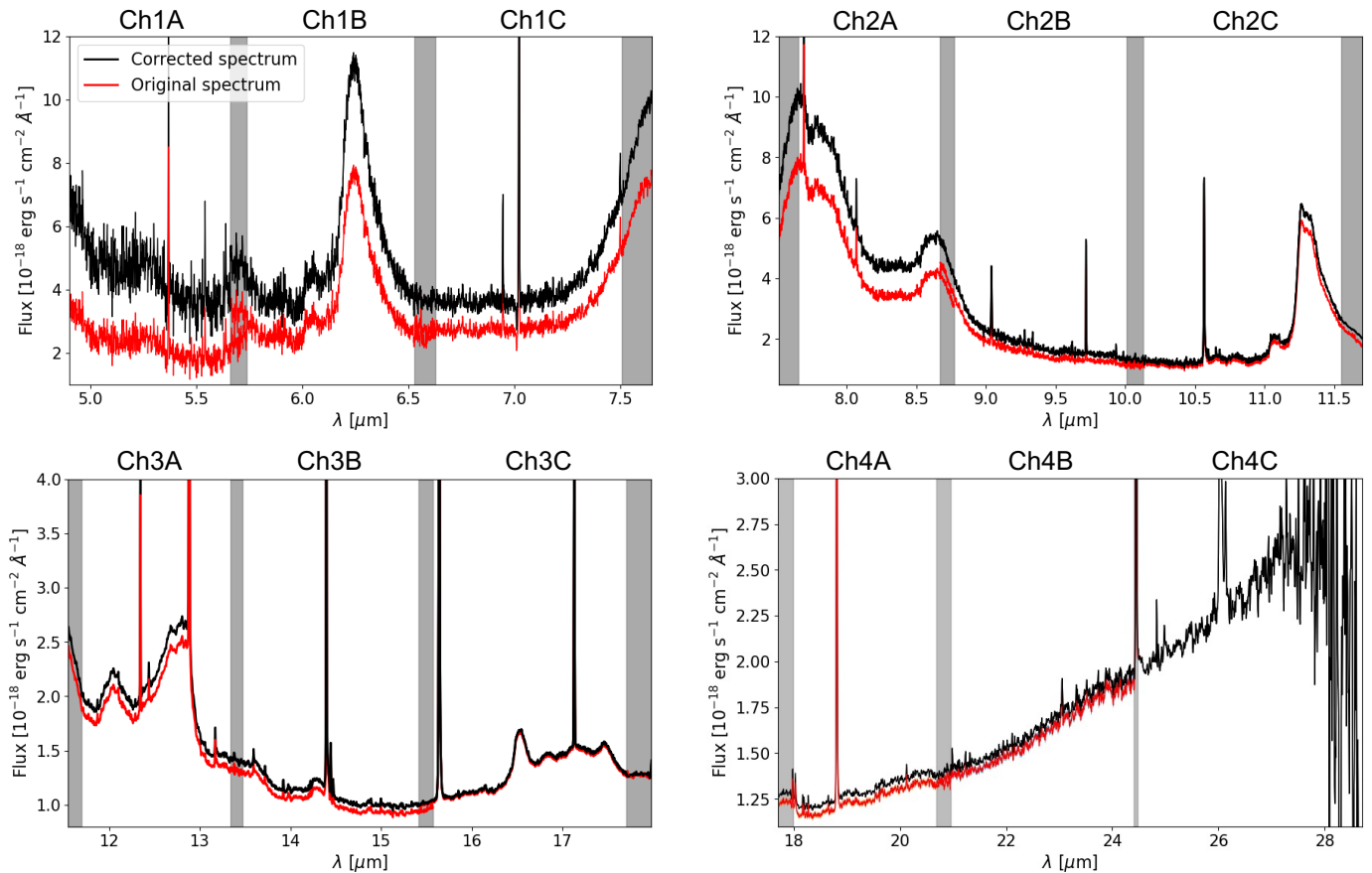


Fig. B.2. Comparison per channel between the original data in red and the stitched data in black. gray regions indicate overlapping spectral channels.

while being allowed to scale in flux. We then subtracted the stellar and nuclear emission from the original unbinned data cube by rescaling the fitted continuum - assumed constant within each Voronoi bin - to match the observed continuum flux in each spaxel, before performing the subtraction.

We obtained continuum-subtracted datacubes containing the gas emission lines only. Then, we repeated the fitting procedure applied for MIRI JWST data (see previous section). In this case, we used up to three Gaussian components to reproduce the complex line profiles and adopted a p -value of 0.9.

Finally, we corrected the optical emission-line fluxes for dust attenuation using the Balmer decrement (i.e., $H\alpha/H\beta$), assuming a case-B hydrogen recombination value of 2.86 for this ratio (for an electron temperature and density of $T_e = 10^4$ K and $n_e = 10^2$ cm^{-3} , respectively; Osterbrock & Ferland 2006) and adopting the Gordon et al. (2023) attenuation law. The results, presented in Appendix D, are consistent with previous estimates by Venturi et al. (2018) and Mingozi et al. (2019). As shown in Fig. D.1, the dust attenuation peaks at $A_V = 3.7$ in the circumnuclear ring, where young stellar clusters are embedded (Liu et al. 2023; Schinnerer et al. 2023). High attenuation values are also found at the nuclear position, while we do not find any correlation of A_V with the outflow morphology, indicative of its low dust content.

Appendix C.3: ALMA emission line fitting

We use the CO(3-2) ALMA observations to derive the kinematics of the cold molecular gas. The continuum was subtracted in

the uv -plane during the data reduction (see Appendix A.3). We fit the CO(3-2) line profile in each spaxel using a single Gaussian profile, which is sufficient to reproduce the symmetric line profile. The resulting moment maps of the cold molecular gas are reported in the bottom panels of Fig. 3.

Appendix D: Extinction and electron density from MUSE

In this appendix, we present the spatially resolved maps of visual extinction and electron density in the circumnuclear region of NGC 1365, derived from the MUSE data and zoomed-in FoV matching the MIRI one. In the top panel of Fig. D.1, we show the visual extinction computed from the Balmer decrement ($H\alpha/H\beta$), adopting the extinction law by Gordon et al. (2023). High visual extinction values of $A_V \sim 3.7$ mag are found at the nuclear position and in the southeastern part of the FoV, corresponding to the circumnuclear ring, as also observed by Venturi et al. (2018) and Mingozi et al. (2019).

Moreover, the bottom panel of Fig. D.1 shows the electron density of the ionized gas, estimated from the total intensity of all the Gaussian components of the $[\text{S II}]\lambda 6716, 6731$ doublet. In particular, we use the $[\text{S II}]\lambda 6716/[\text{S II}]\lambda 6731$ diagnostic line ratio (Osterbrock & Ferland 2006), computed over the same FoV of the Ch4. We assume a typical value for the temperature of ionized gas of $T_e = 10^4$ K and obtain the density map reported in Fig. D.1. We observe that the higher values of n_e are following the outflow morphology, as traced by $[\text{Ne V}]\lambda 14\mu\text{m}$ contours flux. In the main text, we use as average density the median value

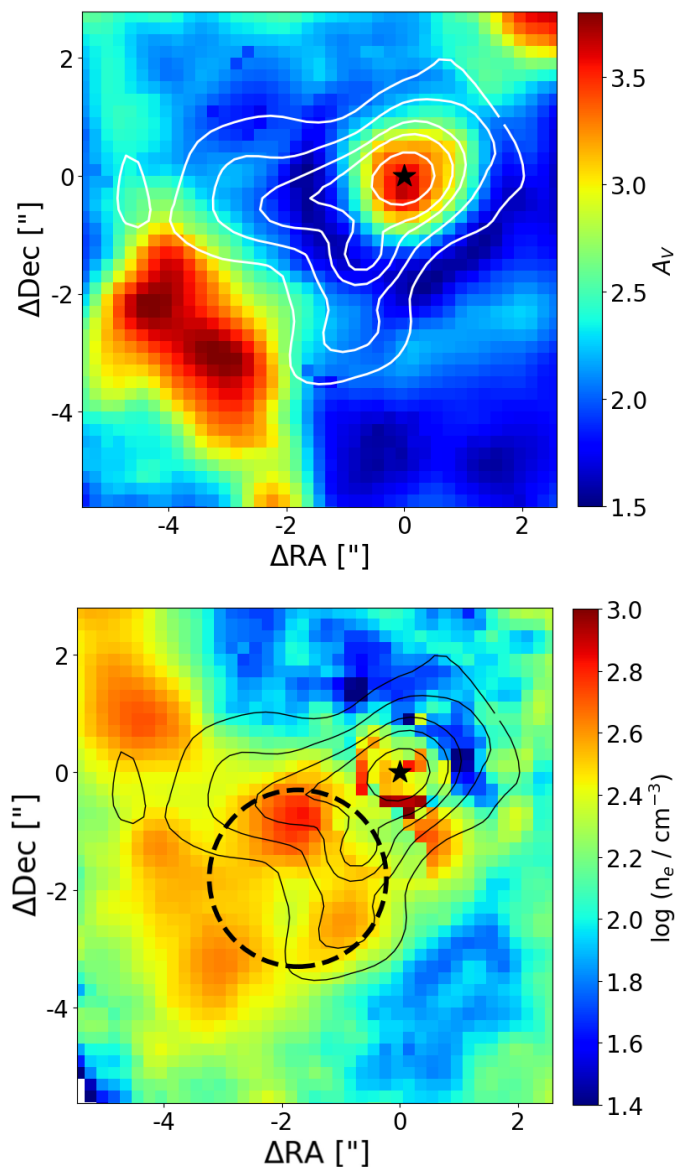


Fig. D.1. Spatially resolved maps of visual extinction and electron density in the circumnuclear region of NGC 1365 obtained from the MUSE data, zoomed in the MIRI FoV. *Top panel:* visual extinction computed from the Balmer decrement. *Bottom panel:* ionized gas electron density obtained from the $[\text{S II}]\lambda 6716/[\text{S II}]\lambda 6731$ line ratio. Contours represent arbitrary flux levels of $[\text{Ne v}]\lambda 14\mu\text{m}$. The black circle marks the $1.5''$ radius aperture used to extract integrated fluxes for the HOMERUN code (see Section 3.5). The star indicates the nucleus position.

and the standard deviation of $n_e = (230 \pm 120) \text{ cm}^{-3}$ measured across the reported FoV.

Appendix E: Density comparison with IRS observations

In this appendix, we compare our spatially resolved JWST/MIRI density measurements with those obtained from integrated spectra by Dudik et al. (2007). Dudik et al. (2007) used the Infrared Spectrograph (IRS) on board *Spitzer* to compute the $[\text{Ne v}]$ ratio in a sample of local AGN. They found that Type 2 AGN show higher line ratios with respect to Type 1, with all Type 2 sources lying above the theoretical LDL threshold, implying $\log(n_e/\text{cm}^{-3}) \leq 2$. In particular, for NGC 1365 they computed a

$[\text{Ne v}]\lambda 24\mu\text{m}/[\text{Ne v}]\lambda 14\mu\text{m}$ ratio of 2.4 ± 0.6 , which is larger than our estimation of 1.0 ± 0.2 obtained as the ratio between the two integrated fluxes in the MIRI FoV. They argued that the $[\text{Ne v}]$ emitting region likely originates inside the nuclear torus and that differential infrared extinction due to dust in the obscuring torus may be responsible for the ratio above the LDL. Exploiting the spatially resolved $[\text{Ne v}]$ emission in our data and the density values in the nuclear region, we can rule out this interpretation. However, given the presence of some LDL regions in Fig. 6, it is possible that their finding is the result of spatial integration over a wide slit, thus including such regions in the measurement. A more plausible reason is an observational effect. Indeed, in Dudik et al. (2007) the $[\text{Ne v}]$ fluxes were obtained using the short-wavelength, high-resolution (SH; $4.7'' \times 11.3''$, $\lambda = 9.9\text{-}19.6 \mu\text{m}$) and long-wavelength, high-resolution (LH; $11.1'' \times 22.3''$, $\lambda = 18.7\text{-}37.2 \mu\text{m}$) modules of IRS. As it is clear from Figure H.5, the extension of $[\text{Ne v}]$ emission is detected up to $8''$ from the nucleus. This means that the SH module surely lost part of the $[\text{Ne v}]\lambda 14\mu\text{m}$ flux, leading to an artificial enhancement of the $[\text{Ne v}]\lambda 24\mu\text{m}/[\text{Ne v}]\lambda 14\mu\text{m}$ line ratio.

Appendix F: HOMERUN emission line fluxes

In this appendix we report the full list of emission lines included in the HOMERUN fit, as shown in Tables F.1 and F.2, and discussed in Section 3.5.3.

Appendix G: Ionized gas mass estimate

In this appendix we present an analytical mass estimation for the $[\text{Ne v}]\lambda 14\mu\text{m}$ and the $[\text{O III}]\lambda 5007\text{\AA}$ emission lines, in order to compute the gas masses in the $1.5''$ radius aperture (shown as a dashed circle in Fig. D.1) and compare them with the HOMERUN estimations in Section 3.5.4.

Following Carniani et al. (2015), we start from the luminosity of the $[\text{Ne v}]\lambda 14\mu\text{m}$ line:

$$L_{[\text{Ne v}]} = \int_V f n_e n(\text{Ne}^{4+}) \gamma_{[\text{Ne v}]}(n_e, T_e) dV \quad (\text{G.1})$$

with f the filling factor, V the volume occupied by the outflowing ionized gas, n_e the electron density, $n(\text{Ne}^{4+})$ the density of Ne^{4+} ions, and $\gamma_{[\text{Ne v}]}(n_e, T_e)$ the line emissivity. $n(\text{Ne}^{4+})$ can be written as

$$n(\text{Ne}^{4+}) = \left[\frac{n(\text{Ne}^{4+})}{n(\text{Ne})} \right] \left[\frac{n(\text{Ne})}{n(\text{H})} \right] \left[\frac{n(\text{H})}{n_e} \right] n_e.$$

We assume $n(\text{Ne}^{4+}) \approx n(\text{Ne})$, $n_e \approx 1.2 n(\text{H})$ (i.e. a 10% number density of He atoms with respect to H atoms), and a solar abundance of $[\text{Ne}/\text{H}] \sim 7.93$ (Asplund et al. 2009), to obtain $n(\text{Ne}^{4+}) \sim 7.09 \times 10^{-5} n_e$. Assuming a typical temperature ($T_e \approx 10^4 \text{ K}$), from the $[\text{Ne v}]\lambda 24\mu\text{m}/[\text{Ne v}]\lambda 14\mu\text{m}$ line ratio we find an electron density of $n_e = (750 \pm 440) \text{ cm}^{-3}$ in the $1.5''$ radius aperture and estimate a line emissivity of $\gamma_{[\text{Ne v}]} = 1.93 \times 10^{-20} \text{ erg s}^{-1} \text{ cm}^3$ making use of PyNeb (Luridiana et al. 2015). Finally, Eq. G.1 can be rewritten as

$$L_{[\text{Ne v}]} = 7.09 \times 10^{-5} f n_e^2 \gamma_{[\text{Ne v}]} V, \quad (\text{G.2})$$

assuming a constant electron density in the outflow volume. The gas mass can be expressed as

$$M = \int_V f \bar{m} n(\text{H}) dV \approx \int_V f m_p n_e dV, \quad (\text{G.3})$$

Table F.1. Optical emission lines fitted by the HOMERUN code

Emission line (1)	Obs. Luminosity (2)	Model (3)	Mod/Obs (4)	AGN frac. (5)	SF frac. (6)	AGN dered. (7)	SF dered. (8)
H β	100.00 \pm 10.00	90.34	0.90	0.76	0.24	302.27	702.62
[O III] λ 5007 \AA	465.99 \pm 46.60	500.05	1.07	0.97	0.04	2022.68	500.44
[N I]* λ 5199 \AA	7.51 \pm 0.75	7.53	1.00	1.00	0.00	29.67	0.00
He II λ 5411 \AA	3.04 \pm 0.32	3.08	1.01	1.00	0.00	11.39	0.00
[Fe VII] λ 5721 \AA	4.77 \pm 0.95	3.64	0.76	1.00	0.00	12.35	0.00
[N II] λ 5755 \AA	2.41 \pm 0.42	2.51	1.04	0.64	0.36	5.37	15.75
[He I]* λ 5876 \AA	19.75 \pm 1.97	19.45	0.99	0.69	0.31	43.90	95.28
[Fe VII] λ 6087 \AA	6.30 \pm 0.63	5.98	0.95	1.00	0.00	18.46	0.00
[O I] λ 6300 \AA	13.55 \pm 1.35	13.68	1.01	0.75	0.25	30.01	43.22
[S III] λ 6312 \AA	1.43 \pm 0.42	1.90	1.33	0.82	0.18	4.55	4.34
[O I] λ 6364 \AA	4.60 \pm 0.46	4.48	0.98	0.75	0.25	9.67	13.81
[Fe X] λ 6375 \AA	1.19 \pm 0.28	1.22	1.03	1.00	0.00	3.53	0.00
H α	622.41 \pm 62.24	660.61	1.06	0.72	0.28	1322.36	2000.05
[N II] λ 6583 \AA	378.71 \pm 37.87	369.45	0.98	0.31	0.69	318.65	2748.56
He I λ 6678 \AA	7.00 \pm 0.70	6.75	0.96	0.62	0.38	11.25	26.74
[S III] λ 6716 \AA	68.33 \pm 6.83	71.35	1.04	0.26	0.74	49.67	535.85
[S III] λ 6731 \AA	63.03 \pm 6.30	52.86	0.84	0.27	0.73	38.19	388.58
[Ar V] λ 7006 \AA	2.07 \pm 0.46	1.72	0.83	1.00	0.00	4.36	0.00
[He I]* λ 7065 \AA	2.56 \pm 25.62	12.78	4.98	0.79	0.21	25.34	22.95
[Ar III] λ 7136 \AA	17.56 \pm 1.76	16.34	0.93	0.61	0.40	24.44	54.04
Ca II λ 7291 \AA	< 1.10	0.00	0.00	0.00	0.00	0.00	0.00
[O III]* λ 7323 \AA	3.11 \pm 0.68	2.87	0.92	0.60	0.40	4.10	8.94
[O III]* λ 7332 \AA	2.41 \pm 0.76	2.35	0.97	0.60	0.40	3.34	7.32
[Ni II] λ 7378 \AA	2.86 \pm 0.43	2.75	0.96	1.00	0.00	6.52	0.00
[Ar III] λ 7751 \AA	4.54 \pm 0.45	4.56	1.00	0.57	0.43	5.80	12.83
[Cl II] λ 8579 \AA	2.48 \pm 0.68	3.52	1.42	0.00	1.00	0.00	17.57
[Fe II] λ 8617 \AA	0.85 \pm 0.67	0.74	0.88	0.51	0.49	0.75	1.79
[S III] λ 9069 \AA	61.72 \pm 6.20	62.49	1.01	0.49	0.52	56.72	140.12

Notes. (1) Name of the emission line. (2) Observed luminosity normalized to an H β flux of 100. For some emission lines, error is set to 1000% to reflect highly uncertain measurements, marginal line detections dominated by noise or simply to exclude those lines from the fit. (3) Line luminosity predicted by the model. (4) Ratio between the model and observed luminosity. (5) Fractional contribution of the AGN component to the observed line luminosity. (6) Fractional contribution of the SF component to the observed line luminosity. (7) Dereddened model luminosity of the AGN component normalized as in column 2. (8) Dereddened model luminosity of the SF component normalized as in column 2.

where the average molecular weight is $\bar{m} = 1.27 m_p$, if there is a 10% fraction of He atoms, and we have taken into account that

$$\bar{m} n(H) = \bar{m} \left[\frac{n(H)}{n_e} \right] n_e = 1.27 m_p (1.2)^{-1} n_e \approx m_p n_e, \quad (\text{G.4})$$

therefore, $M \approx f m_p n_e V$. Combining this latter with Equation G.2, we finally get

$$M_{[\text{Ne V}]} = 3.07 M_\odot \left(\frac{L_{[\text{Ne V}]}}{10^{36} \text{ erg s}^{-1}} \right) \left(\frac{n_e}{200 \text{ cm}^{-3}} \right)^{-1}. \quad (\text{G.5})$$

Similarly, we compute the [O III] λ 5007 \AA outflow mass. Using a solar abundance of [O/H] \sim 8.69 (Asplund et al. 2009) and $n_e = (500 \pm 270) \text{ cm}^{-3}$ (from the [S II] λ 6716, 6731 ratio in the same aperture) - that leads to $\gamma_{[\text{O III}]} = 3.53 \times 10^{-21} \text{ erg s}^{-1} \text{ cm}^3$ - we have

$$M_{[\text{O III}]} = 2.92 M_\odot \left(\frac{L_{[\text{O III}]}}{10^{36} \text{ erg s}^{-1}} \right) \left(\frac{n_e}{200 \text{ cm}^{-3}} \right)^{-1}. \quad (\text{G.6})$$

We corrected both the [Ne V] λ 14 μm and the [O III] λ 5007 \AA luminosity for dust attenuation using the Balmer decrement from

the H α /H β ratio, employing the Gordon et al. (2023) attenuation law and an intrinsic ratio H α /H β = 2.86 (for T $_e$ = 10 4 K, Osterbrock & Ferland 2006). Assuming the two different densities for the optical and mid-IR species previously computed, we obtain an outflow mass of M $_{[\text{Ne V}]} = (2.6 \pm 1.0) \times 10^3 M_\odot$ and M $_{[\text{O III}]} = (20 \pm 7) \times 10^4 M_\odot$.

Appendix H: Moment maps

In this appendix, we present the moment maps of H $_2$, recombination, low IP, medium IP, and high IP emission lines from Fig. H.1 to Fig. H.5, respectively.

Table F.2. Mid-IR emission lines fitted by the HOMERUN code

Emission line	Obs. Luminosity	Model	Mod/Obs	AGN frac.	SF frac.	AGN dered.	SF dered.
(1)	(2)	(3)	(4)	(5)	(6)	(7)	(8)
[Fe II] λ 5 μ m	140.58 \pm 14.06	129.03	0.92	0.16	0.84	21.24	116.24
[Fe VII] λ 5 μ m	14.01 \pm 140.07	6.92	0.49	1.00	0.00	7.12	0.00
[Mg VII] λ 5 μ m	17.20 \pm 2.79	18.04	1.05	1.00	0.00	18.57	0.00
[Mg V] λ 5 μ m	95.37 \pm 9.54	82.35	0.86	1.00	0.00	84.74	0.00
[Ni II] λ 6 μ m	8.30 \pm 0.99	8.57	1.03	1.00	0.00	8.82	0.00
[Fe II] λ 6 μ m	6.28 \pm 62.75	9.37	1.5	0.16	0.84	1.54	8.43
[Ar II] λ 7 μ m	384.47 \pm 3844.69	72.16	0.19	0.04	0.96	2.97	74.35
[Na III] λ 7 μ m	16.93 \pm 1.69	19.32	1.14	1.00	0.00	19.96	0.00
Pa α	25.02 \pm 2.50	24.06	0.96	0.36	0.64	9.02	16.62
[Ne VI] λ 7 μ m	222.70 \pm 22.27	235.62	1.06	1.00	0.00	244.35	0.00
[Fe VIII] λ 7 μ m	4.22 \pm 1.32	6.01	1.43	1.00	0.00	6.25	0.00
[Ar V] λ 8 μ m	8.34 \pm 1.18	8.63	1.04	1.00	0.00	8.99	0.00
[Na VI] λ 8 μ m	11.93 \pm 119.32	5.41	0.45	1.00	0.00	5.74	0.00
[Ar III] λ 9 μ m	97.69 \pm 9.77	112.34	1.15	0.22	0.78	26.98	104.45
[Na IV] λ 9 μ m	12.77 \pm 1.28	12.67	0.99	1.00	0.00	13.70	0.00
[Fe VII] λ 9 μ m	15.73 \pm 1.57	15.87	1.01	1.00	0.00	17.55	0.00
[S IV] λ 10 μ m	426.55 \pm 42.66	453.92	1.06	0.95	0.05	474.43	25.76
Hu α	7.82 \pm 0.78	8.60	1.10	0.36	0.64	3.24	6.15
[Ne II] λ 13 μ m	974.91 \pm 97.49	944.99	0.97	0.02	0.98	23.79	1022.99
[Ar V] λ 13 μ m	16.32 \pm 1.63	14.11	0.87	1.00	0.00	14.74	0.00
[Mg V] λ 13 μ m	4.97 \pm 0.50	5.53	1.11	1.00	0.00	5.77	0.00
[Ne V] λ 14 μ m	389.91 \pm 38.99	339.14	0.87	1.00	0.00	353.89	0.00
[Cl II] λ 14 μ m	19.20 \pm 1.92	17.49	0.91	0.00	1.00	0.00	19.33
[Na VI] λ 14 μ m	9.54 \pm 0.95	8.36	0.88	1.00	0.00	8.73	0.00
[Ne III] λ 16 μ m	593.28 \pm 59.33	543.72	0.92	0.71	0.29	401.92	177.98
[Fe II] λ 18 μ m	10.99 \pm 1.10	12.65	1.15	0.19	0.81	2.59	11.53
[S III] λ 18 μ m	386.66 \pm 38.67	360.72	0.93	0.24	0.77	89.40	312.78
[Fe VI] λ 19 μ m	8.76 \pm 0.88	8.94	1.02	1.00	0.00	9.42	0.00
[Fe III] λ 23 μ m	17.24 \pm 1.72	16.91	0.98	0.31	0.69	5.54	13.03
[Ne V] λ 24 μ m	388.76 \pm 38.88	442.87	1.14	1.00	0.00	463.94	0.00
[O IV] λ 26 μ m	1535.40 \pm 153.54	1278.60	0.83	1.00	0.00	1337.12	0.01
[Fe II] λ 26 μ m	57.59 \pm 11.52	45.21	0.79	0.20	0.80	9.43	40.19

Notes. See Table F.1.

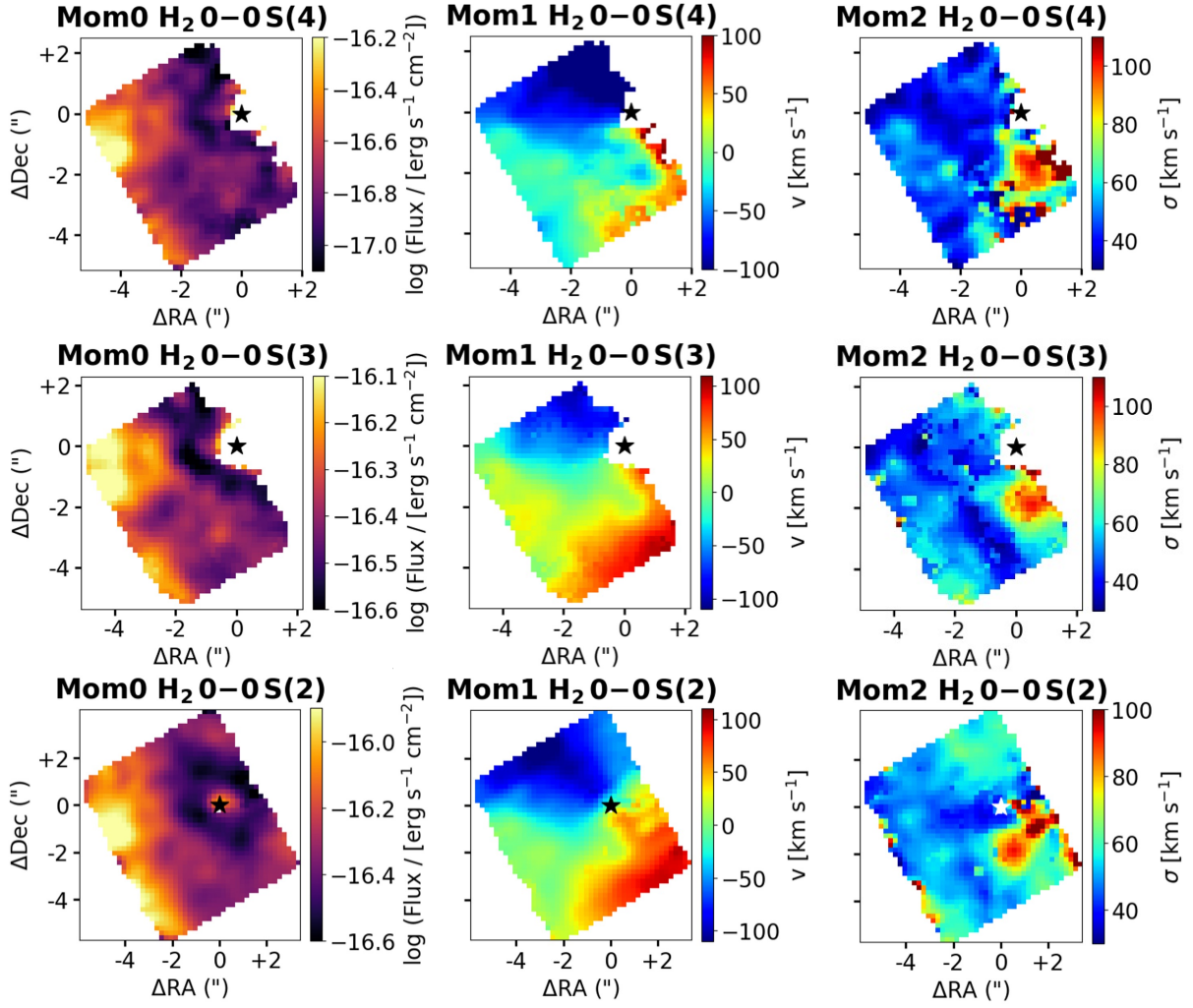


Fig. H.1. Moment maps of H₂ emission lines. From left to right, we plot the flux map, the velocity map, and the velocity dispersion map. Star indicates nucleus position. Spaxels with SNR < 5 are masked out.

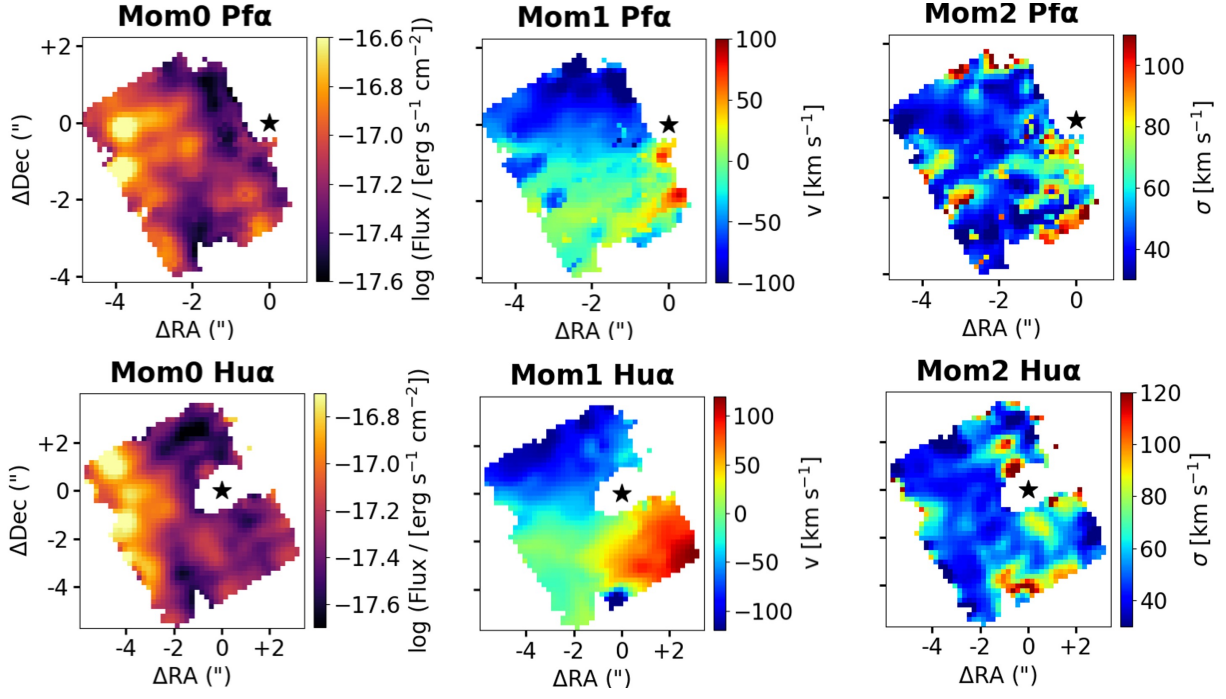


Fig. H.2. Continue of Fig. H.1 for recombination emission lines.

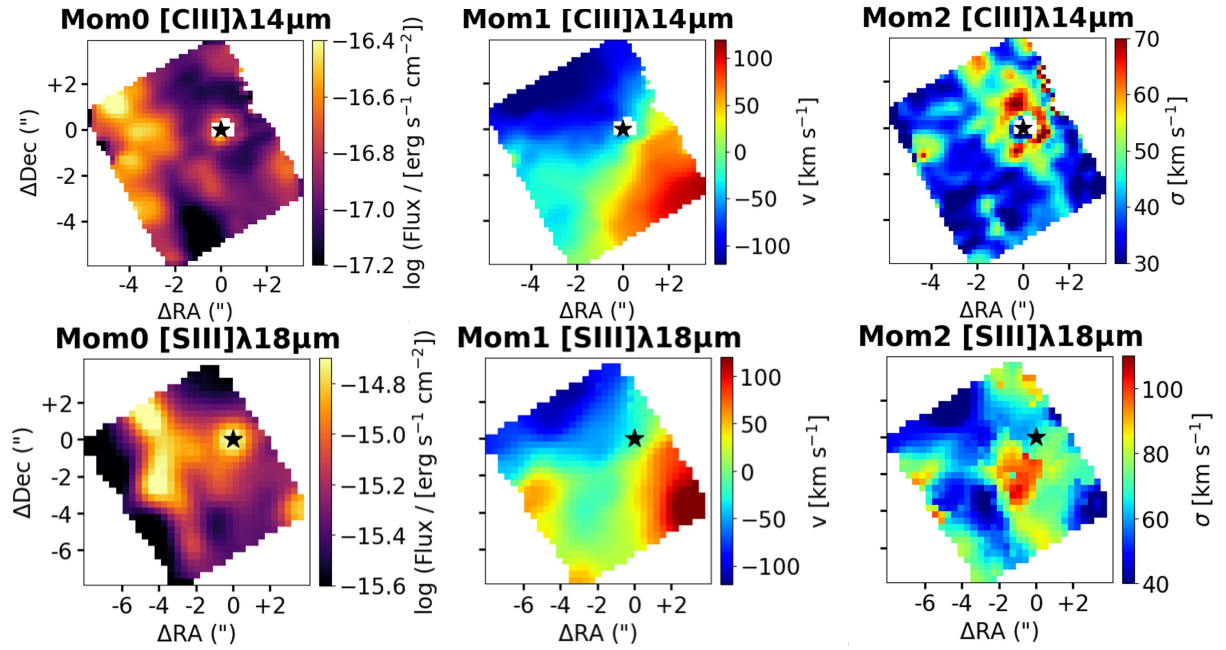


Fig. H.3. Continue of Fig. H.1 for low IP emission lines.

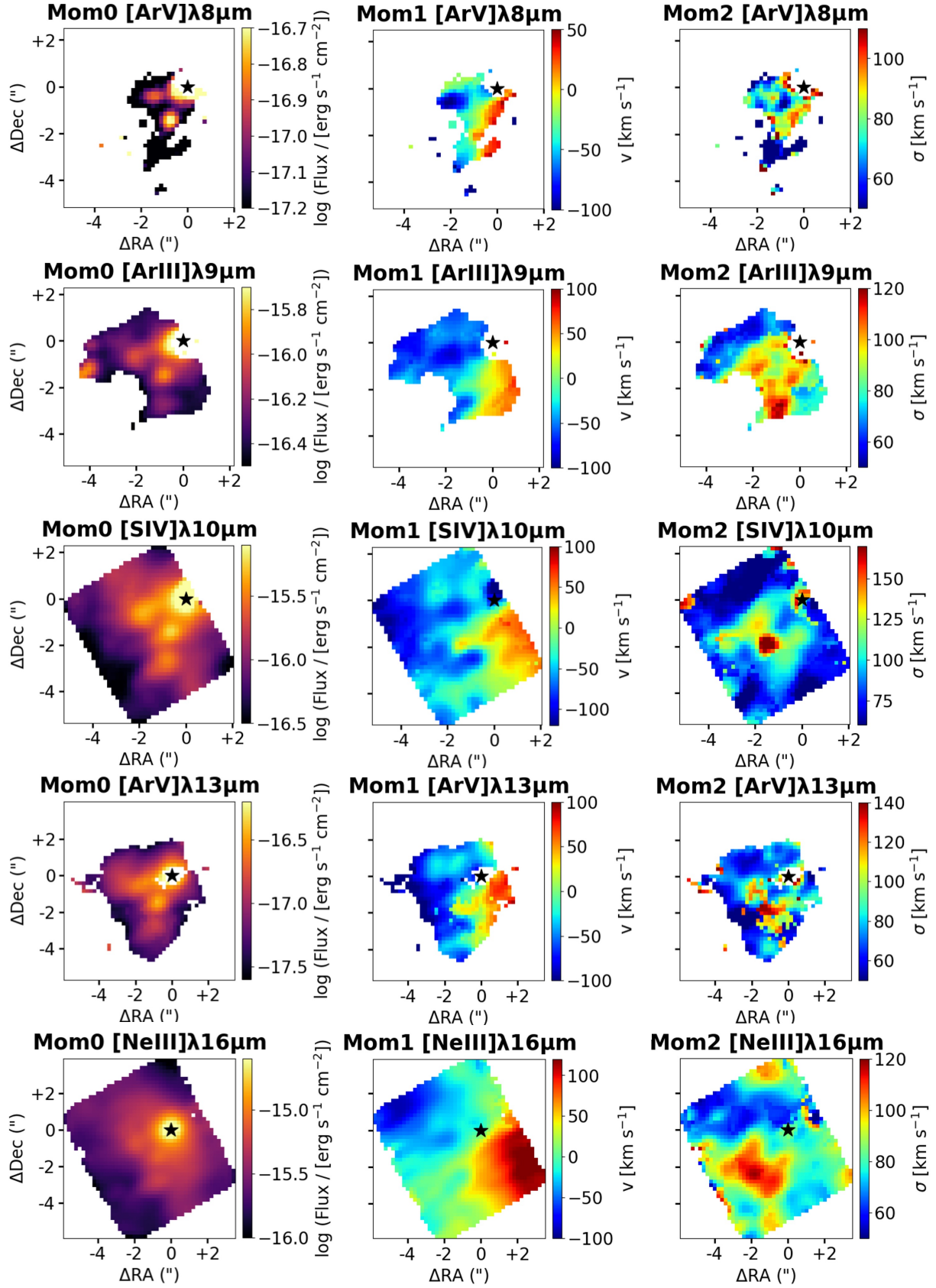


Fig. H.4. Continue of Fig. H.1 for medium IP emission lines.

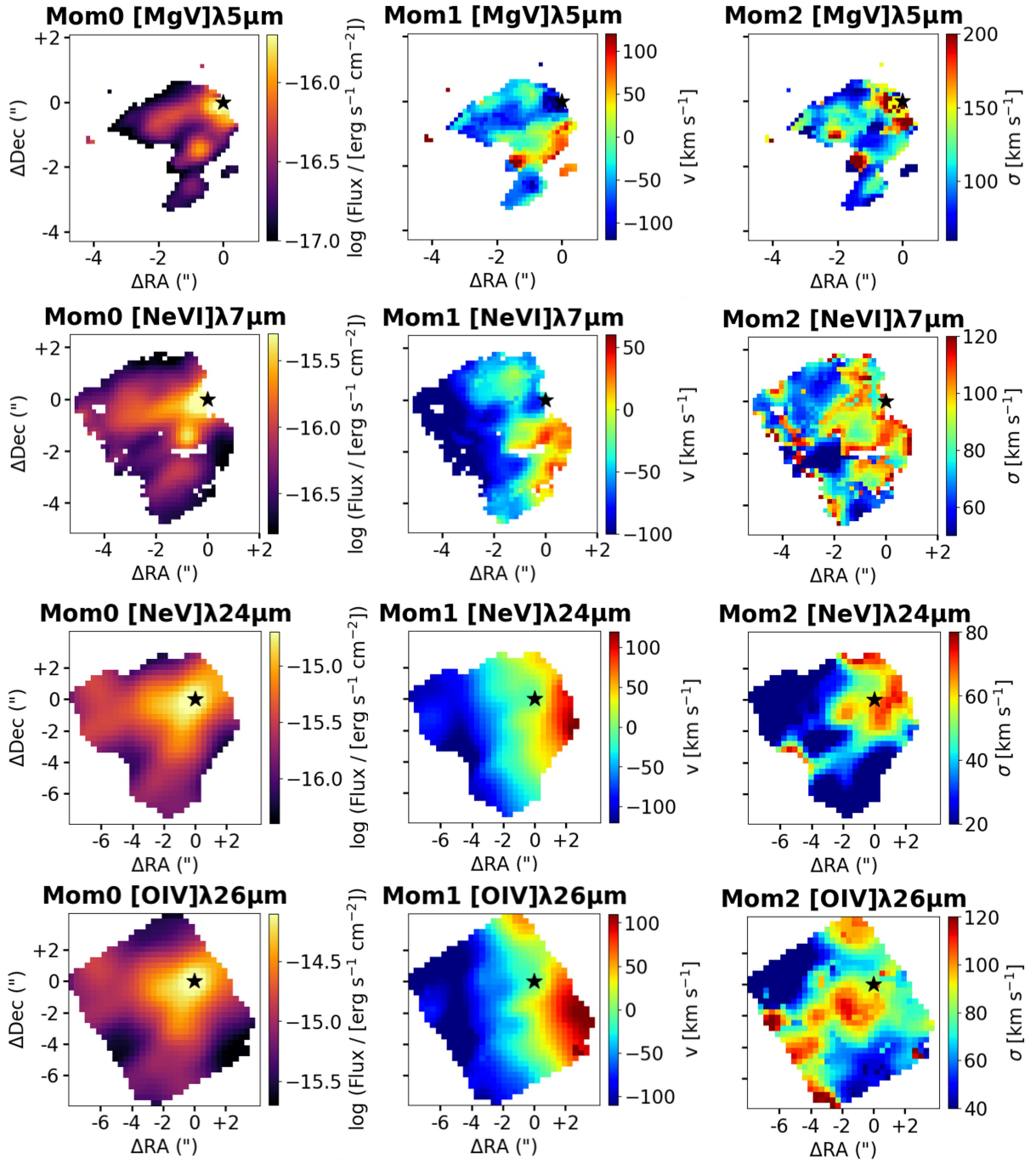


Fig. H.5. Continue of Fig. H.1 for high IP emission lines.